Journal of Power Sources 647 (2025) 237306

Contents lists available at ScienceDirect

Journal of Power Sources

journal homepage: www.elsevier.com/locate/jpowsour

MoOC-Mo_2C/C heterojunction enables fast water dissociation for efficient alkaline hydrogen evolution reaction

Yulei Ren [a], Xuming Zhang [a,*], Hao Song [a,**], Chaoran Pi [a], Jianping Li [a], Xingju Liu [c], Chan Lin [c], Pengcheng Wei [c], Zhuo Li [a,***], Paul K. Chu [b]

[a] The State Key Laboratory of Refractories and Metallurgy and Institute of Advanced Materials and Nanotechnology, Wuhan University of Science and Technology, Wuhan, 430081, China
[b] Department of Physics, Department of Materials Science and Engineering, and Department of Biomedical Engineering, City University of Hong Kong, Tat Chee Avenue, Kowloon, Hong Kong, China
[c] Guizhou Wujiang Hydropower Development Co, LTD, Guiyang, 550002, China

HIGHLIGHTS

- MoOC-Mo_2C heterojunction is formed by thermal reduction of carbon-intercalate MoO_x.
- Oxygen incorporation boosts water adsorption and dissociation at MoOC-Mo_2C interface.
- The MoOC-Mo_2C heterojunction exhibits strong electron coupling effects.
- The MoOC-Mo_2C catalyst shows excellent HER activity in alkaline and seawater.

ARTICLE INFO

Keywords:
Carbide
Oxycarbide
Interface engineering
Heterostructure
Hydrogen evolution reaction

ABSTRACT

The advancement of non-precious electrocatalysts with high efficiency is crucial for the industrial implementation of the hydrogen evolution reaction (HER). In non-acidic environments, the dissociation of water and interactions between hydrogen and the catalyst are pivotal. This research presents a novel hybrid electrocatalyst, comprising a molybdenum oxycarbide and carbide heterojunction integrated onto carbon cloth (MoOC-Mo_2C/C), which is fabricated through in situ interface engineering. The MoOC-Mo_2C catalyst demonstrates exceptional electrical conductivity and remarkable HER performance across a wide pH range, particularly in alkaline conditions, as exemplified by Tafel slope of 38 mV dec^{-1}, an ultralow overpotential of 45 mV at a current density of 10 mA cm^{-2}, and notable long-term stability. Both experimental findings and theoretical analyses suggest that the incorporation of oxygen into the carbide structure enhances water adsorption and lowers the energy barrier for water dissociation. Furthermore, the distinct work functions of MoOC and Mo_2C facilitate effective electron transfer from MoOC to Mo_2C, optimizing the energy of hydrogen adsorption and significantly enhancing the activity and kinetics of alkaline HER. Our results underscore the promising potential of this highly efficient non-precious electrocatalyst, which exhibits a pronounced affinity for water molecules, in facilitating hydrogen evolution in alkaline media.

1. Introduction

Hydrogen is a promising, sustainable, and efficient energy carrier because of its zero carbon emission and high energy density [1,2]. Electrocatalytic water splitting powered by renewable energy sources represents a viable technological approach for hydrogen production [3,4]. Although precious metal-based electrocatalysts have exceptional efficiency in hydrogen production, their high cost and limited availability hinder broader commercial implementation [5,6]. During water splitting, the oxygen evolution reaction (OER) in alkaline environments

* Corresponding author.
** Corresponding author.
*** Corresponding author.
E-mail addresses: xumzhang@wust.edu.cn (X. Zhang), songhao201809@wust.edu.cn (H. Song), zhuo_li@wust.edu.cn (Z. Li).

https://doi.org/10.1016/j.jpowsour.2025.237306
Received 26 January 2025; Received in revised form 11 March 2025; Accepted 7 May 2025
Available online 11 May 2025

exhibits significant advantages, thus necessitating the development of cost-effective, non-precious metal electrocatalysts for the alkaline hydrogen evolution reaction (HER) to complement the alkaline OER [7–9]. Among the various transition metal catalysts, carbides like MoC and Mo_2C are promising alternatives due to their distinctive Pt-like electronic properties, excellent corrosion resistance, and metallic-like conductivity. Therefore, the synthesis of efficient Mo_xC-based electrocatalysts is vital to achieving superior HER performance in industrial hydrogen production.

It is well known that the ratio of Mo to C in Mo_xC influences the electronic properties and electron delocalization states, which in turn affect the adsorption of H*. For instance, Mo_2C has a high hydrogen binding energy, while MoC shows less favorable Mo-H interactions and inadequate H* adsorption [10,11]. Recent research shows that the Mo_xC-based heterostructured electrocatalyst comprising MoC and Mo_2C phases can improve the electrocatalytic HER activity on account of the tailored *d*-band structure at the interface, which enables efficient H^+ catalytic conversion and hydrogen desorption [12,13]. These overpotentials are better than those of their individual counterparts. However, the catalytic activity of the Mo_xC heterostructure remains inferior to that of precious metals in alkaline media, primarily due to the weak water affinity, which impedes rapid water dissociation.

The incorporation of oxygen into a non-oxide catalyst is a promising strategy to enhance the water affinity and promote water dissociation on catalysts. For example, Wen et al. have prepared an O-doped layered NiCoP/Ni_2P hybrid electrode by phosphatization and dip coating. The introduction of O optimizes the free energy of hydrogen and water absorption, accelerates the alkaline HER process, and achieves a small overpotential of 58 mV at 10 mA cm^{-2} while maintaining long-term stability [14]. Similarly, Yang et al. have synthesized O-coordinated W-Mo heterodimers in N-doped graphene, in which electron delocalization in W-O-Mo-O-C optimizes the adsorption of H* and the adsorption energy of water at the active site, thereby enhancing HER kinetics and intrinsic activity [15]. Consequently, it is plausible to anticipate that the introduction of oxygen into Mo_xC-based heterostructures can bolster their interaction with water molecules and promote efficient HER in alkaline environments. The precise fabrication of oxygenated carbides presents significant difficulties, as the excessive introduction of oxygen leads to the formation of oxide phases. While these oxide phases can improve hydrophilicity, the resultant high electron delocalization contributes to increased electrochemical resistance, thereby impeding hydrogen desorption [16–18]. In this regard, the meticulous synthesis of O-doped Mo_xC-based heterostructures, along with a deeper comprehension of the catalytic mechanisms involved, is essential for advancement, despite the inherent challenges.

This study presents an innovative approach for the synthesis of MoOC-Mo_2C/C heterostructures on carbon cloth through precision phase engineering. The MoOC phase is generated by subjecting the precursors of carbon-intercalated layered MoO_x (MoO_x/C) nanobelt arrays (NBAs) to low-temperature annealing in an Ar/H_2 atmosphere. Subsequently, the lattice oxygen within the MoOC is selectively extracted at elevated annealing temperatures, leading to the *in-situ* formation of the MoOC-Mo_2C heterojunction. Both experimental findings and theoretical evaluations indicate that the MoOC-Mo_2C heterojunction exhibits significant electron coupling phenomena at the interfaces, while the elevated electronic state of MoOC-Mo_2C at the Fermi level enhances water adsorption and dissociation, thereby improving hydrogen desorption kinetics. Electrochemical assessments demonstrate that the catalyst achieves remarkable alkaline HER performance, rivaling that of commercial Pt/C catalysts, underscoring its promising potential for practical hydrogen production.

2. Experimental section

2.1. Materials

Ammonium molybdate ($(NH_4)_6Mo_7O_{24}\cdot4H_2O$, ≥99 %) and anhydrous N,N-dimethylformamide (DMF, ≥99.9 %) were purchased from Aladdin Ltd. Commercial RuO_2 and 20 wt% Pt/C were obtained from Civi-Chem. Carbon cloth (CC, WOS1011) was purchased from Taiwan CeTech Co., Ltd.

2.2. Synthesis of MoOC/C, Mo_2C/C, and MoOC-Mo_2C/C nanobelt arrays (NBs)

The MoOC-Mo_2C/C NBs were prepared by annealing the MoO_x/C NBs precursors at 600 °C, 700 °C and 800 °C for 2 h under flowing H_2/Ar atmosphere at a heating rate of 5 °C min^{-1} (products denoted as MoOC-Mo_2C/C-600, MoOC-Mo_2C/C-700, and MoOC-Mo_2C/C-800, respectively). The MoOC/C NBs and Mo_2C/C NBs were produced at 500 °C and 900 °C under the same conditions. In this paper, the MoOC-Mo_2C/C-700 sample annealed at 700 °C is designated as MoOC-Mo_2C/C.

2.3. Synthesis of NiFe-LDH nanosheets on nickel foam

Typically, the cleaned nickel foam (NF) (1 × 2 cm^2) was immersed into 80 mL of 0.4 M $Fe(NO_3)_3$, then the nickel foam was removed and dried for further use. Once again, the Ni foam (NF) was immersed in 50 mL 2.5 M NaOH, after drying, rinsed with deionized water for several times, and NiFe-LDH was obtained after drying.

2.4. Materials characterization

The crystal structure of the samples was detected by X-ray diffraction (XRD), and the test results were analyzed by SmartLab Studio II. The micromorphology of the samples was characterized by scanning electron microscopy (SEM) and transmission electron microscopy (TEM). X-ray photoelectron spectrometer (XPS) and Raman scatterer (LabRAM HR) were used to analyze the surface chemical state of the samples. The work function of the samples was analyzed by ultraviolet photoelectron spectrometer (Thermo ESCALAB 250XI).

2.5. Theoretical calculation

In the DFT theory calculations, the Mo_2C(101), MoOC(111), and Mo_2C(101)-MoOC(111) plate models were established according to characterization results. The vacuum layer along the z direction was 15 Å to weaken the effect between the images. The method of VASP and projected augmentation wave (PAW) is used for the calculation. Perdew-Burke-Ernzerhof (PBE) functional and DFT-D3 correction were used to optimize the model. The cutoff energy of the plane wave base is set to 450 eV. The Brillouin region is integrated with A K-point grid of 0.03 $Å^{-1}$ to ensure the rational optimization of the crystal structure. Electron energy optimization is confirmed when the energy change is less than the convergence energy threshold of 10^{-5} eV. The maximum stress per atom is within 0.02 eV $Å^{-1}$, and the geometry and lattice constant optimization results are considered to be internal.

3. Results and discussion

Fig. 1 schematically illustrates the preparation process of the MoOC-Mo_2C/C nanobelt arrays (NBs). After the hydrothermal reaction in the DMF solution containing ammonium heptamolybdate tetrahydrate, the hybrid NBs precursor grows uniformly on carbon cloth (CC) (Fig. S1). Subsequently, the hybrid precursor is pyrolyzed at 500 °C for 1 h in an Ar atmosphere to obtain MoO_x/C nanobelts (Fig. S2). Subsequent annealing in an Ar/H_2 environment facilitates the synthesis of MoOC/C and MoOC-Mo_2C/C nanobelts, ultimately leading to the production of

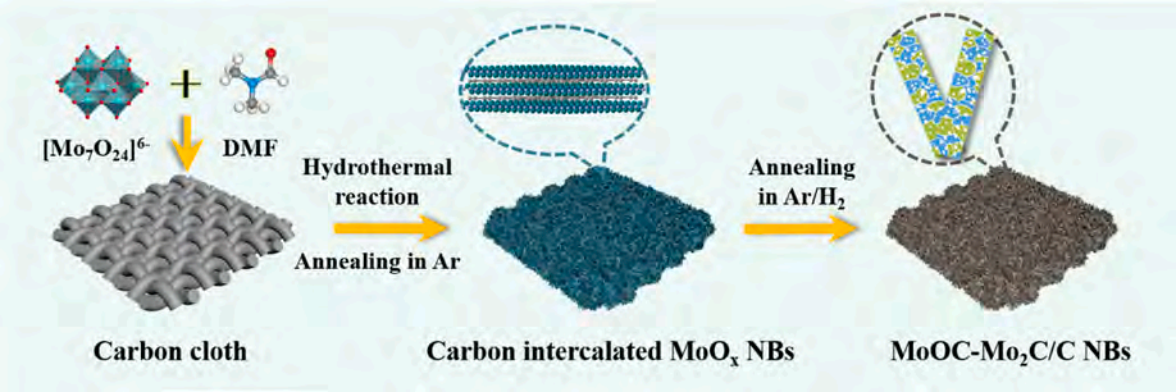

Fig. 1. Illustration of the preparation procedures of MoOC-Mo_2C/C NBs/CC.

pure-phase Mo_2C/C nanobelts exhibiting analogous morphology upon elevating the annealing temperatures (Fig. S3). The MoOC-Mo_2C/C-700 sample annealed at 700 °C is designated as MoOC-Mo_2C/C. Based on our previous report, carbothermal reduction is the essential process for producing MoOC/C and Mo_2C from MoO_x/C [19].

The X-ray diffraction (XRD) pattern (Fig. 2a) reveals that after the treatment at 500 °C, the graphite carbon peak appears at 26.3°. The diffraction peaks at 37.6°, 43.6°, 63.5°, and 76.3° are attributed to the (111), (200), (220), and (311) planes of cubic MoOC (PDF# 17–0104). In an Ar/H_2 atmosphere, diffraction peaks corresponding to the MoOC phase and Mo_2C (PDF# 35–0787) are observed with the increase of annealing temperature, and no obvious impurities are detected, confirming the successful preparation of the MoOC/Mo_2C composite (Fig. S4). Raman scattering is performed to monitor the structural evolution mechanism from MoOC to Mo_2C (Fig. S5). The Raman peaks at 666, 819, and 996 cm^{-1} stem from Mo-C in molybdenum carbide [20], and that at 560 cm^{-1} originates from oxygen vacancies [21], which gradually recede during conversion from MoOC to Mo_2C, in addition to weaker Mo-O (726 cm^{-1}) and Mo-O-C (892 cm^{-1}) bands [22,23]. The D peak (1346 cm^{-1}) and G peak (1590 cm^{-1}) indicate the existence of graphitic carbon [24,25], and the intensity decreases gradually when the structure changes from MoOC/C to Mo_2C/C, demonstrating the important role of lattice oxygen extraction. As shown by the small-angle XRD patterns in Fig. S6, the hydrothermal precursor exhibits the (010), (020), and (030) diffraction peaks indicative of the layer-by-layer structure composed of the organic precursors and MoO_x. The (010) peak undergoes a high-angle shift at the high calcination temperature of 500 and 700 °C in argon, suggesting a reduction in interlayer spacing after pyrolysis of the organic intercalated compound. The layered structure favors carbon substitution of lattice oxygen in MoO_x. The morphology and crystal structure of MoOC-Mo_2C/C are examined by SEM and TEM. As shown in Fig. 2b-c, MoOC-Mo_2C/C with a length of approximately 5 μm and a diameter of 150 nm is well-arranged on the CC substrate, and the partial transformation of oxide into carbide results in volumetric shrinkage and produces a rougher surface of the NBs. The NBs with uniformly dispersed pores with sizes of 5–10 nm facilitate

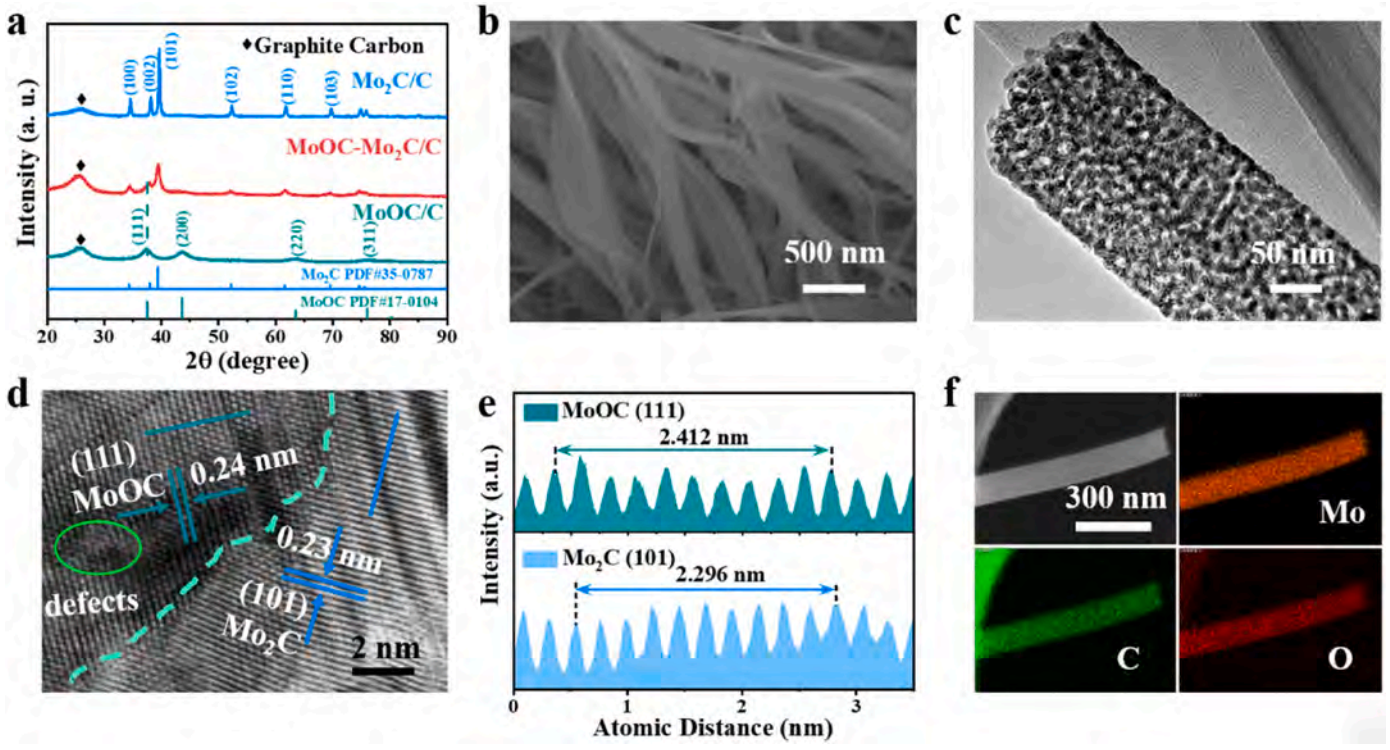

Fig. 2. (a) XRD patterns; (b, c) SEM and TEM images and (d) HR-TEM image of MoOC-Mo_2C/C NBs; (e) Pixel atomic distances of the MoOC (111) plane and Mo_2C (101) plane extracted from the corresponding HR-TEM image; (f) EDS elemental maps of MoOC-Mo_2C/C.

contact with the electrolyte during HER and expose abundant catalytic sites [26]. Fig. 2d shows the HR-TEM image of MoOC-Mo_2C/C. The results show that lattice fringe spacings of 0.23 nm and 0.24 nm arising from the (101) facet of hexagonal Mo_2C and the (111) facet of cubic MoOC, respectively, which are confirmed by the intensity profiles across the lattice planes in Fig. 2e. The homogeneous distributions of Mo, O, and C in MoOC-Mo_2C/C are verified by EDS (Fig. 2f).

X-ray photoelectron spectroscopy (XPS) is carried out to probe the interfacial electronic interactions in the MoOC/Mo_2C. Fig. 3a shows the high-resolution Mo 3*d* XPS spectra of MoOC/C and MoOC-Mo_2C/C. The fitted peaks corresponding to $Mo^{\delta+}$ species ($3< \delta < 6$) with binding energies of 230.1 and 233.3 eV in MoOC/C are attributed to C-O-Mo bonds [27,28], and the high oxidation state of Mo^{6+} can be inferred from the peaks at 232.2 and 235.4 eV for MoO_3. With regard to MoOC--Mo_2C/C, the binding energy of $Mo^{\delta+}$ in the MoOC counterpart exhibits a positive shift of 0.2 eV, and the fitted doublets at 231.9 eV/228.7 eV and 231.3 eV/228.1 eV correspond to Mo^{3+} and Mo^{2+} in Mo_2C [29], suggesting electron dissipation in MoOC at the MoOC/Mo_2C interface. Fig. 3b shows the C 1*s* peak of MoOC-Mo_2C/C, with the peak at 284.4 eV assigned to C-O-Mo in oxycarbide, representing a positive shift of 0.3 eV compared with pure MoOC [20]. And the peaks corresponding to C=O, C-O, C-C, and C-Mo appear at 288.5, 286.0, 284.6, and 283.4 eV, respectively [30,31]. Fig. 3c shows the O 1*s* spectra. The three peaks at 530.4, 531.6, and 533.2 eV stem from Mo-O, oxygen vacancies, and C-O/C=O [32,33]. Similarly, the Mo-O peak of MoOC-Mo_2C/C exhibits a positive shift of 0.15 eV relative to MoOC/C. The Mo 3*d* to C 1*s* area ratio for Mo_2C and MoOC increases, while oxygen vacancies diminish gradually as MoOC is converted into Mo_2C. The findings indicate that the oxygen vacancies present in pristine MoOC and Mo_2C, which contain lower-valence metal cations, arise from a phase transition induced by in situ oxygen extraction. Consequently, the pronounced electronic interactions between MoOC and Mo_2C enhance the optimization of their electronic structures [34].

To further characterize the change in the band structure and interfacial charge polarization between MoOC and Mo_2C, ultraviolet photoelectron spectra (UPS) are acquired from MoOC and Mo_2C (Fig. 3d). The work functions of MoOC and Mo_2C are 5.16 and 5.43 eV, respectively. Surface-sensitive UPS (Fig. 3e) is performed to study the occupied electronic states of MoOC-Mo_2C/C with reference to MoOC/C and Mo_2C/C. The valence band maximum of MoOC-Mo_2C/C upshifts to 3.18 eV compared to 2.76 eV of Mo_2C/C and 2.92 eV of MoOC/C, suggesting a downshift of E_d [35,36]. Based on the *d*-band theory, the antibonding states of hydrogen may downshift to the Fermi Level (E_f), consequently weakening the interactions between the H* and MoOC-Mo_2C interfacial

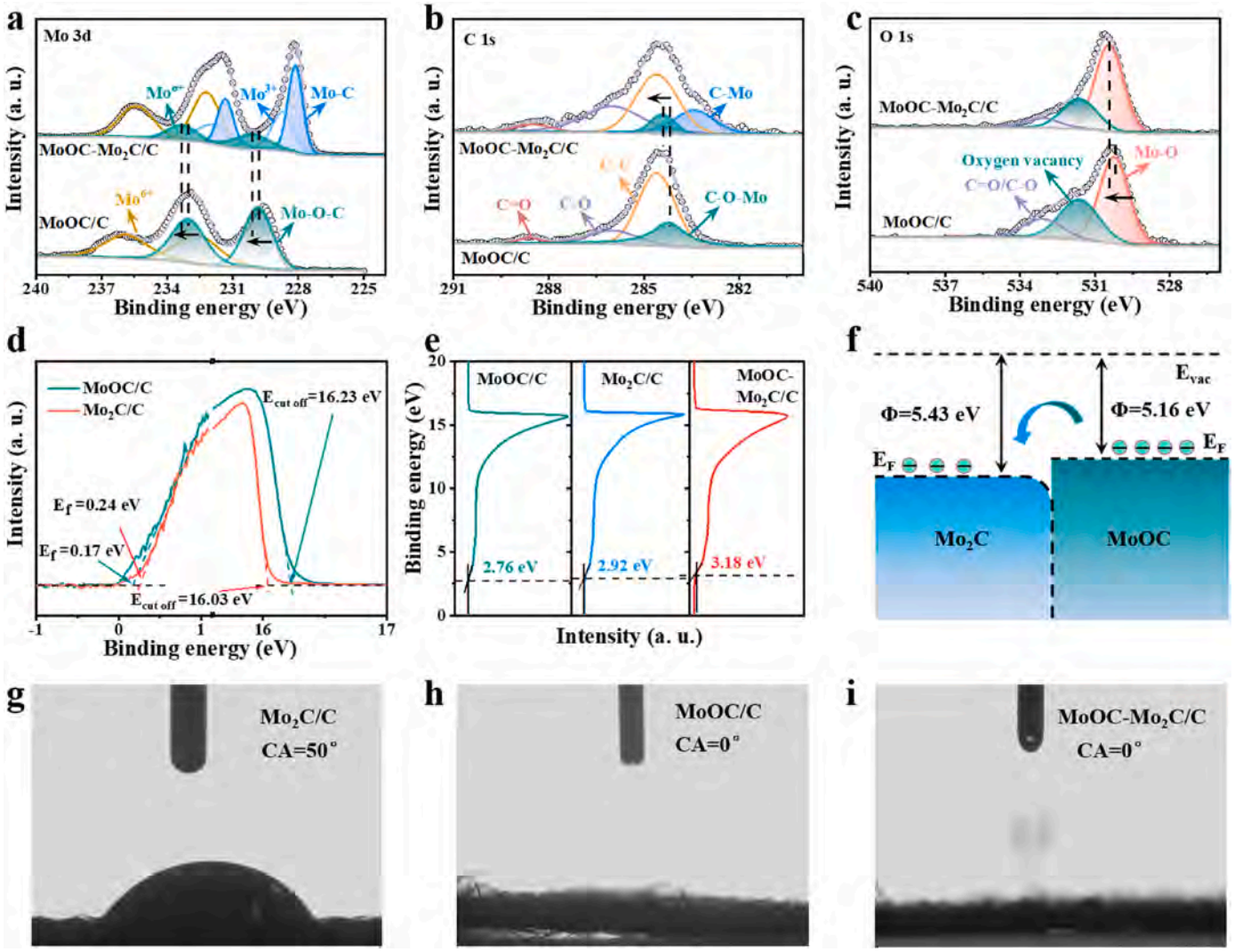

Fig. 3. High-resolution XPS spectra of (a) Mo 3d, (b) C 1s and (c) O 1s of MoOC/C and MoOC-Mo_2C/C; (d) UPS spectra and (e) Valence-band spectra (VBS) of MoOC/C, MoOC-Mo_2C/C, and Mo_2C/C; (f) Schematic diagram of electron transfer and corresponding energy band diagrams of Mo_2C/C and MoOC/C. The hydrophilicity tests of (g) Mo_2C/C, (h) MoOC/C and (i) MoOC-Mo_2C/C.

sites to boost the HER kinetics. Based on the UPS and Surface-sensitive UPS results, an energy band structure diagram (Fig. 3f) is plotted to demonstrate that owing to the difference in work function between MoOC and Mo_2C, electrons flow spontaneously from the higher energy level to the lower energy level during contact until an equilibrium state is reached. This electron transfer regulates charge separation and promotes the desorption of hydrogen intermediates. Moreover, the hydrophilicity of the electrode surface also influences the kinetics of HER performance. To analyze the effect of introducing oxygen into Mo_2C on its hydrophilicity, contact angle measurements were conducted. The results in Fig. 3g-i show that the contact angles of the Mo_2C/C and MoOC/C electrodes are 40° and 0°, respectively, while the contact angle of Mo_2C-MoOC/C is close to 0°. This indicates that the introduction of oxygen significantly improves the hydrophilicity of Mo_2C, making it easier for the electrolyte to reach the active catalytic center during the electrochemical catalysis process. This enhanced wettability is likely to contribute to the improved HER performance in the MoOC-Mo_2C/C catalyst.

The electrocatalytic HER characteristics of the MoOC/C, heterojunction MoOC-Mo_2C/C, and Mo_2C/C electrodes are determined on a three-electrode system. In this system, the Hg/HgO electrode (in 1 M KOH) serves as the reference electrode, and a graphite rod is used as the counter electrode. For comparison, the commercial Pt/C (20 wt%) catalyst with the same mass loading on CC is also evaluated. The polarization curves are corrected automatically by 85 % iR-compensation. Fig. 4a-b displays the linear sweep voltammetry (LSV) plots of the samples in 1 M KOH. MoOC-Mo_2C/C has excellent catalytic activity showing 45 mV at 10 mA cm^{-2}. This performance is comparable to that of Pt/C, which shows a potential of 40 mV, and significantly better than MoOC/C (82 mV) and Mo_2C/C (119 mV). Furthermore, at large current densities of 500 and 1000 mA cm^{-2}, the overpotentials of MoOC-Mo_2C/C are 256 and 427 mV, respectively, which are much lower than those of Pt/C (412 and 703 mV) and other reference samples (Fig. S7). The Tafel slope of MoOC-Mo_2C/C is 38 mV dec^{-1}, which is lower than those of MoOC/C (55 mV dec^{-1}) and Mo_2C/C (63 mV dec^{-1}) and close to that of Pt/C (35 mV dec^{-1}) (Fig. 4c), suggesting fast reaction kinetics [37]. The enhanced HER activity clearly demonstrates that H_2O dissociation and H_2 release are promoted by the heterojunction MoOC-Mo_2C. The exchange current density (j_0) of the optimal MoOC--Mo_2C/C catalyst is calculated to be 0.72 mA cm^{-2}, which is twice that of MoOC/C (0.30 mA cm^{-2}) and seven times larger than Mo_2C/C (0.11 mA cm^{-2}), further demonstrating the high activity of MoOC-Mo_2C/C (Fig. S8). Electrochemical active surface area (ECSA) was used to evaluate the electrocatalytic behavior of the materials. The regular rectangular shape observed from the CV curve indicates the typical electrical double-layer capacitive behavior. Fig. S9 shows that the CV curves of Mo_2C/C are more rectangular than those of MoOC/C, but the ECSA of MoOC/C is 103 mF cm^{-2} and larger than that of Mo_2C/C (56 mF cm^{-2})

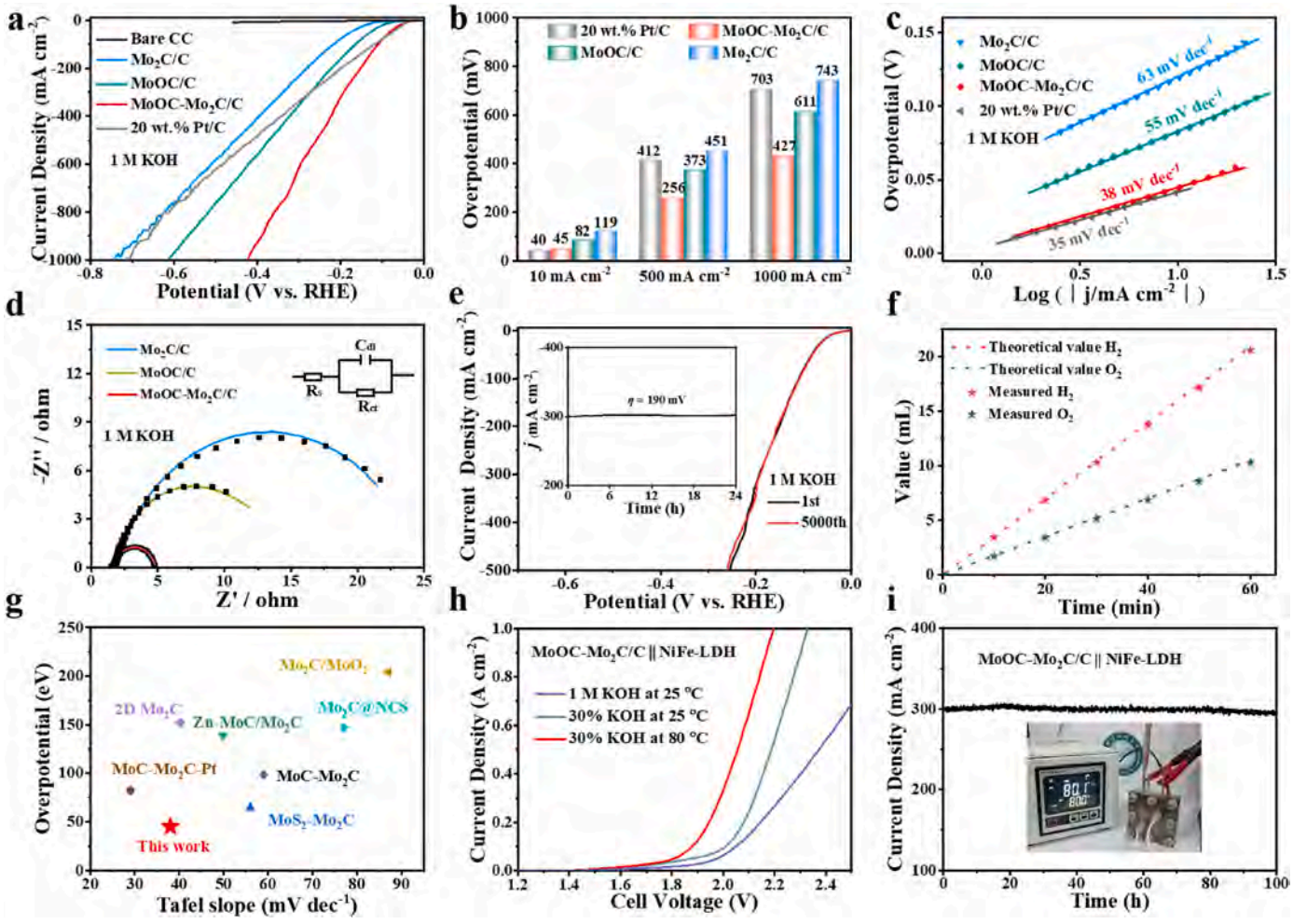

Fig. 4. (a) Polarization curves of CC, Mo_2C/C, MoOC/C, MoOC-Mo_2C/C, and commercial 20 wt% Pt/C in 1 M KOH; (b) Overpotentials and (c) Tafel plots of different electrodes; (d) Nyquist plots of MoOC/C, Mo_2C/C, and MoOC-Mo_2C/C-700 in 1 M KOH; (e) Polarization curves of MoOC-Mo_2C/C at the beginning and after 5000 cycles in 1 M KOH with the inset showing the i-t curve of MoOC-Mo_2C/C; (f) Faradaic efficiency of HER and OER; (g) Comparison of MoOC-Mo_2C/C with other reference electrocatalysts in 1 M KOH; (h) Steady polarization curves and (i) Chronopotentiometry results of MoOC-Mo_2C/C of the MEA device at initial 300 mA cm^{-2}.

because the compact double electric layer with more adsorbed water on MoOC decreases the thickness of the double electric layer. Electrochemical impedance spectroscopy (EIS) shows that the change transfer resistance (R_{ct}) of MoOC-Mo_2C/C is 3.1 Ω cm^2, which is smaller than those of MoOC/C, Mo_2C/C and other reference samples (Table S1 and Fig. 4d), implying fast interfacial charge transfer kinetics in HER. The turnover frequency (TOF) of MoOC-Mo_2C/C is 0.798 s^{-1} at an overpotential of 350 mV, which is larger than those of MoOC/C (0.484 s^{-1}) and Mo_2C/C (0.425 s^{-1}) (Fig. S10), indicating that MoOC-Mo_2C/C has higher catalytic activity. The HER characteristics of the MoOC-Mo_2C/C catalyst in acidic and neutral solutions are assessed. As shown in Fig. S11a–b, the LSV curves of MoOC-Mo_2C/C exhibit overpotentials of 92 mV and 89 mV at a current density of 10 mA cm^{-2} in 0.5 M H_2SO_4 and 1 M PBS, respectively, which are much lower than those of MoOC/C (123 and 105 mV) and Mo_2C/C (151 and 127 mV). The Tafel slopes of MoOC-Mo_2C/C are 61 and 58 mV dec^{-1} under acidic and neutral solutions, respectively, and less than those of MoOC/C (74 and 72 mV dec^{-1}) and Mo_2C/C (75 and 75 mV dec^{-1}) (Fig. S11c–d). The CV curves of the catalyst under acidic and neutral conditions exhibit similar patterns (Fig. S12). In addition, the C_{dl} values of the optimal MoOC-Mo_2C/C are 72 and 94 mF cm^{-2} in acidic and neutral media, which exceed those of Mo_2C/C (51 and 63 mF cm^{-2}) and less than those of MoOC/C (95 and 112 mF cm^{-2}) (Fig. S13a–b). In acidic and neutral solutions with an overpotential of 150 mV, the TOF values of MoOC-Mo_2C/C are 0.076 and 0.053 s^{-1}, respectively, which are better than Mo_2C/C and MoOC/C (Fig. S13c–d). These results indicate that MoOC-Mo_2C/C has excellent electrocatalytic activity in a wide range of pH. After 5000 CV cycles in 1 M KOH, the polarization curves of MoOC-Mo_2C/C show no shift (Fig. 3e and S14), and there is almost no decline in the cathodic current density after performing chronopotentiometry at 110 mV for 24 h (inset in Fig. 4e) confirming the outstanding stability. After the long-term assessment, MoOC-Mo_2C/C retains the pristine crystal phase and nanobelt morphology (Fig. S15). The chemical states of O_v, C 1*s*, and Mo 3*d* determined by XPS show no changes compared to the pristine sample (Fig. S16). In the HER process, the Faradaic efficiency of the MoOC--Mo_2C/C catalyst is approximately 98.4 % at 50 mA cm^{-2} for 60 min (Fig. 4f). All in all, the optimal MoOC-Mo_2C/C sample delivers excellent HER performance that is comparable to that of Pt/C and surpasses that of many similar Mo-based hybrid electrocatalysts in alkaline solutions in terms of the overpotentials as well as Tafel slopes. The results are summarized in Fig. 4g–Table S2 and S3.

The practicality of the MoOC-Mo_2C/C catalyst is evaluated to demonstrate its commercial potential [38]. The overall water-splitting electrolyzer is assembled with the MoOC-Mo_2C/C cathode and NiFe LDH anode in alkaline (1 M KOH) and alkaline seawater electrolytes (1 M KOH + 0.5 M NaCl). The preparation and OER properties of FeNi-LDH are presented in Fig. S17 and S18. The MoOC-Mo_2C/C catalyst shows excellent corrosion resistance against chloride during HER (Fig. S19). Fig. S20 shows that the MoOC-Mo_2C/C||NiFe-LDH electrolyzer needs only 1.513 and 1.523 V to drive 10 mA cm^{-2} in the alkaline and alkaline seawater electrolytes, respectively, which are lower than those of the benchmark Pt/C||RuO_2 electrolyzer (1.542 V and 1.562 V). As a proof of concept, the membrane electrode assembly (MEA) electrolyzer, which is a two-electrode device for overall water splitting, is assembled with a

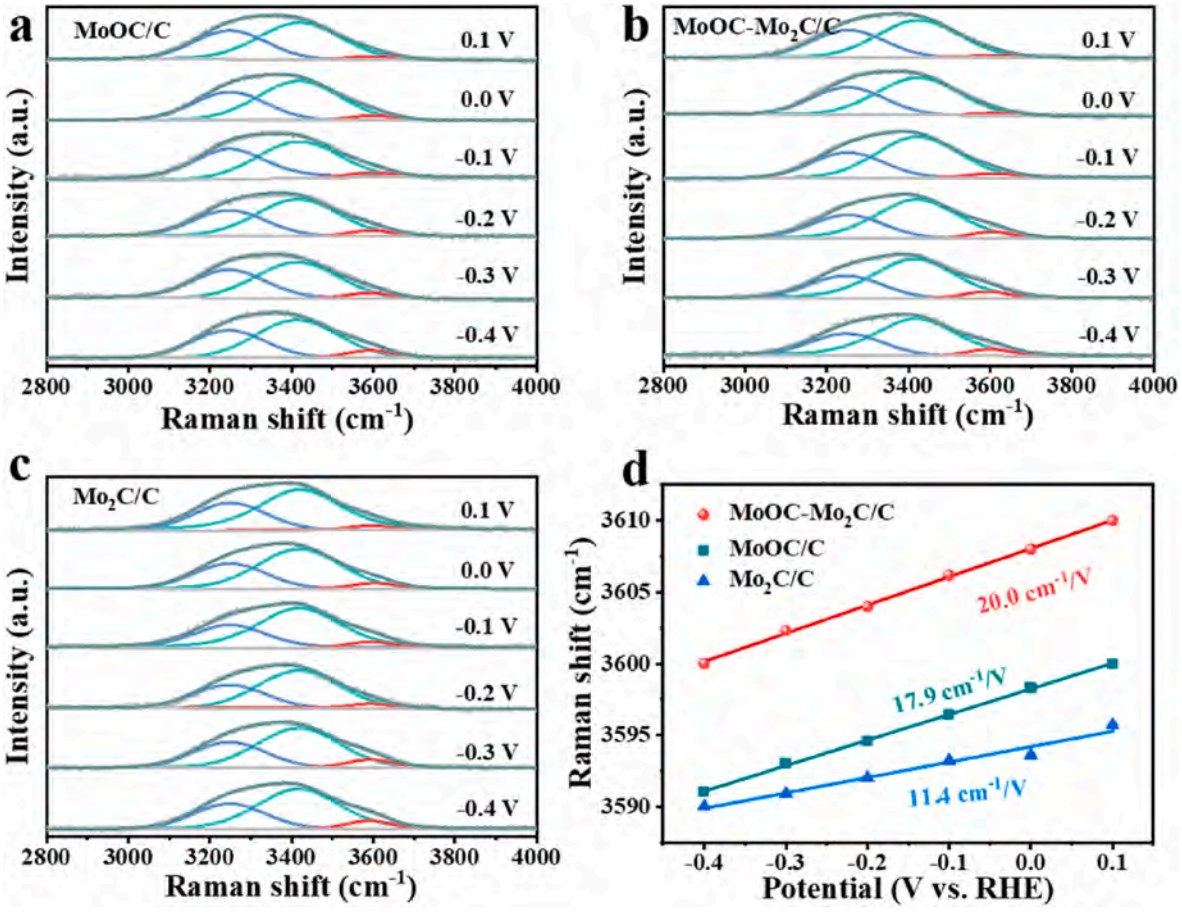

Fig. 5. In situ Raman spectra of interfacial water on (a) MoOC/C, (b) MoOC-Mo_2C/C and (c) Mo_2C/C electrode in a 0.1 M NaOH solution. Gaussian fits of three O-H stretching modes are shown in blue, cyan and red, respectively; (d) Frequency plots of O-H stretching mode changes in the interfacial water Raman spectra of MoOC/C, MoOC-Mo_2C/C, and Mo_2C/C in 0.1 M NaOH.. (For interpretation of the references to colour in this figure legend, the reader is referred to the Web version of this article.)

MoOC-Mo_2C/C cathode and a NiFe-LDH anode for alkaline conditions (1 M KOH and 30 % KOH). The MEA (MoOC-Mo_2C/C) exhibits higher catalytic activity exemplified by a current density of 1 A cm^{-2} at 2.33 V and 2.19 V in 30 % KOH at room temperature and 80 °C (Fig. 4h). The performance metric of electrolyzer is significantly superior to that of Mo-based catalysts in Table S4. As shown in Fig. 4i, MoOC-Mo_2C/C exhibits excellent stability during water splitting at a current density of 300 mA cm^{-2} for 100 h, indicating promising prospects in practical applications.

In order to further understand the dynamic changes in the electrode/solution interface of MoOC-Mo_2C/C during HER, in situ Raman scattering is carried out. As shown in Fig. 5a-c, distinct O-H stretching vibration of H_2O is observed in the range between 3000 and 3800 cm^{-1} during HER (from 0.1 V to – 0.6 V). The vibration peaks stem from 4-coordinated hydrogen-bonded water (4-HB•H_2O), 2-coordinated hydrogen-bonded water (2-HB•H_2O), and Na^+ ion hydrated water (Na^+•H_2O) [2,40]. As the voltage decreases, the Stark effect associated with Na^+•H_2O is observed by fitting the shifts of the vibration peaks. The Stark slope of MoOC-Mo_2C/C is 20.0 cm^{-1}/V, which is larger than those of MoOC (17.9 cm^{-1}/V) and Mo_2C/C (11.4 cm^{-1}/V), indicating that MoOC-Mo_2C/C is sensitive to Na^+•H_2O and promotes the adsorption of interfacial water (Fig. 5d). In addition, the closer proximity of free water at the interface contributes to efficient electron transport and boosts the HER activity.

To study the underlying mechanism responsible for the high catalytic activity of MoOC-Mo_2C, DFT calculation is conducted [39]. Based on the XRD and HR-TEM observations, the MoOC (111)-Mo_2C (101) surface is selected as the optimal model for the MoOC-Mo_2C heterostructure, and the MoOC (111) and Mo_2C (101) surfaces are compared (Fig. S21). The evaluation of catalytic activity involves calculating the intricate pathway in HER, including the adsorption of H_2O, the dissociation of H_2O, and the adsorption and desorption of H* to form H_2. The binding energies of H_2O with MoOC, Mo_2C, and MoOC-Mo_2C/C are −1.014, −0.687, and −1.314 eV, respectively (Fig. 6a), indicating that

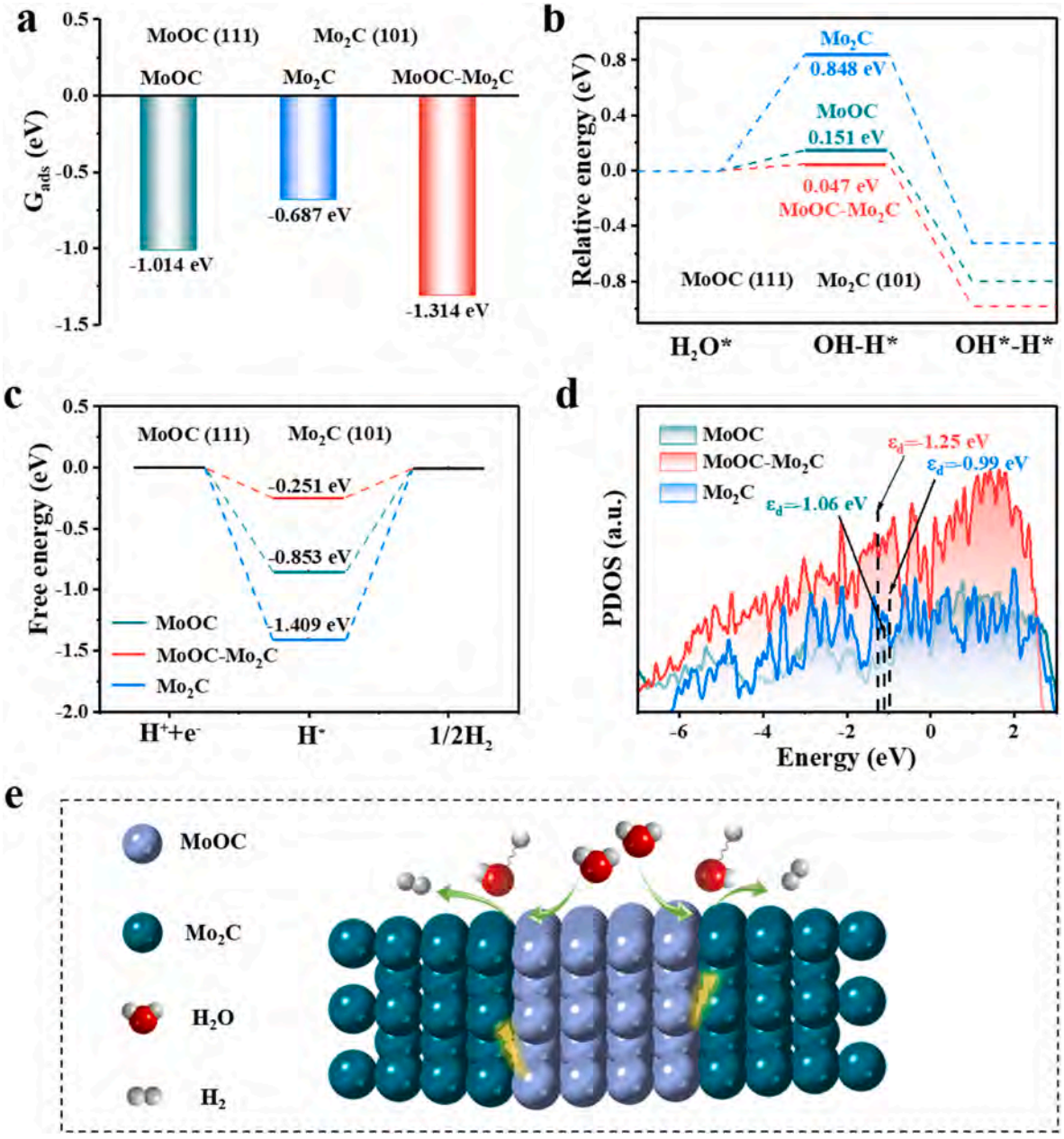

Fig. 6. (a) H_2O adsorption on MoOC, Mo_2C, and MoOC-Mo_2C; (b) H_2O dissociation energy on MoOC, Mo_2C, and MoOC-Mo_2C; (c) Gibbs free energies of H* on MoOC, Mo_2C, and MoOC-Mo_2C; (d) Projected density of states (PDOS) distributions of MoOC, MoOC-Mo_2C, and Mo_2C; (e) Schematic illustration of the HER mechanism.

MoOC-Mo_2C/C is more favorable to H_2O adsorption than MoOC or Mo_2C, thus driving the dissociation of H_2O. This finding is consistent with the conclusions derived from the hydrophilicity tests of the samples. Fig. 6b displays the Gibbs free energies of H_2O dissociation ($E_{OH^*\text{-}H^*}$) of MoOC, Mo_2C, and MoOC-Mo_2C/C in HER. The $E_{OH\ \text{-}H^*}$ values of MoOC and MoOC-Mo_2C/C are 0.048 and 0.063 eV, respectively, indicating that both of them can effectively dissociate H_2O. The ΔG_{H^*} values of MoOC and MoOC-Mo_2C/C are −0.853 and −0.251 eV, respectively (Fig. 6c), suggesting that the H* intermediate adsorbs spontaneously onto MoOC despite a significant barrier for H_2 desorption. With regard to MoOC-Mo_2C/C, the substantial increase of ΔG_{H^*} favors H_2 desorption, so that the spontaneous electron transfer at the interface improves the H_2 desorption of MoOC-Mo_2C/C. The projected density of states (PDOS) distribution is calculated to study the electronic structures of Mo_2C and MoOC. Compared to Mo_2C, the 2*p* orbital of lattice O atoms and C atoms around E_f shows strong interactions with the 4*d* orbital of Mo atoms in MoOC (Fig. S22). In addition, the density of states at the Fermi level of MoOC-Mo_2C/C is similar to that of MoOC and higher than that of MoOC and Mo_2C, indicating that the MoOC-Mo_2C/C heterostructure has higher conductivity than MoOC (Fig. 6d). The abundant electrons at the interface interact with $Na^+\bullet H_2O$ to affect water migration and adsorption. The *d*-band centers (E_d) of MoOC-Mo_2C/C, MoOC, and Mo_2C are at −1.25, −1.06, and −0.99 eV relative to the E_f, respectively. The E_d value of the MoOC-Mo_2C/C heterostructure is farther away from the Fermi level, indicating smaller antibonding energy and weaker interactions between H* and MoOC-Mo_2C interfacial sites, thereby favoring H desorption and HER kinetics. Overall, the energy barrier for hydrogen adsorption/desorption at the MoOC-Mo_2C interface decreases due to the adjustment of the *d*-band center. As a result, the MoOC-Mo_2C interface exhibits better HER activity than both MoOC and Mo_2C in a wide pH range (Fig. 6e).

4. Conclusion

In summary, the MoOC-Mo_2C heterojunction catalyst is fabricated through meticulous phase engineering via the reduction of carbon-intercalated layered MoO_x nanosheets. The MoOC-Mo_2C/C catalyst has rich heterogeneous interfaces and delivers efficient and stable HER performance in a wide pH range, particularly in alkaline conditions, outperforming the majority of previously reported Mo_xC-based catalysts. Both experimental findings and theoretical calculations indicate that the regulation of the *d*-band center through electron transfer as a result of work function adjustments improves the adsorption of hydrogen intermediates on MoOC-Mo_2C/C, thereby promoting HER activity. Importantly, MoOC-Mo_2C/C exhibits exceptional electrocatalytic efficacy and stability in simulated seawater and membrane electrode assembly (MEA) devices. This study reveals a simple strategy to modify molybdenum carbide catalysts by introducing an interstitial oxygen microenvironment, highlighting that the optimization of the electronic structure of molybdenum carbide catalysts is vital for the advancement of advanced catalysts for energy generation and storage.

CRediT authorship contribution statement

Yulei Ren: Writing – original draft, Methodology, Investigation, Formal analysis, Data curation. **Xuming Zhang:** Writing – review & editing, Resources, Project administration, Conceptualization. **Hao Song:** Writing – original draft, Investigation, Formal analysis, Data curation. **Chaoran Pi:** Methodology, Data curation. **Jianping Li:** Investigation, Data curation. **Xingju Liu:** Resources. **Chan Lin:** Resources. **Pengcheng Wei:** Resources. **Zhuo Li:** Writing – review & editing, Supervision, Conceptualization. **Paul K. Chu:** Writing – review & editing, Resources.

Declaration of competing interest

The authors declare that they have no known competing financial interests or personal relationships that could have appeared to influence the work reported in this paper.

Acknowledgements

This work was financially supported by the National Natural Science Foundation of China (22379116 and 22309056), and City University of Hong Kong Donation Research Grants (DON-RMG 9220061 and 9229021). The authors are grateful for the facility support provided by the Analytical & Testing Center of Wuhan University of Science and Technology.

Appendix A. Supplementary data

Supplementary data to this article can be found online at https://doi.org/10.1016/j.jpowsour.2025.237306.

Data availability

Data will be made available on request.

References

[1] W. Zhang, L. Yang, Z. Li, G. Nie, X. Cao, Z. Fang, X. Wang, S. Ramakrishna, Y. Long, L. Jiao, Regulating hydrogen/oxygen species adsorption via built-in electric field-driven electron transfer behavior at the heterointerface for efficient water splitting, Angew. Chem. Int. Ed. 63 (2024) 202400888, https://doi.org/10.1002/ange.202400888.

[2] Y. Feng, N. Ran, X. Wang, Q. Liu, J. Wang, L. Liu, K. Suenaga, W. Zhong, R. Ma, J. Liu, Nanoparticulate WN/Ni_3C coupling in ceramic coatings for boosted urea electro-oxidation, Adv. Energy Mater. 13 (2023) 2302452, https://doi.org/10.1002/aenm.202302452.

[3] M. Mushtaq, Z. Zhu, H. Yang, Z. Khanam, Y. Hu, S. Mathi, Z. Wang, M. Sadeeq Balogun, Y. Huang, Lattice strain-modulated trifunctional $CoMoO_4$ polymorph-based electrodes for asymmetric supercapacitors and self-powered water splitting, Small 21 (2024) 2409418, https://doi.org/10.1002/smll.202409418.

[4] Y. He, M. Tu, W. Gan, Z. Zhu, M. Mushtaq, M. Al-Mamun, J. Deng, H. Yang, Z. Wang, M. Sadeeq Balogun, Efficient alkaline freshwater/seawater hydrogen production via heterogeneous N-doped $FeMoO_4$/Mo_2N rod-shaped electrocatalysts, ChemSusChem (2024) e202401425, https://doi.org/10.1002/cssc.202401425.

[5] M. Zhou, X. Jiang, W. Kong, H. Li, F. Lu, X. Zhou, Y. Zhang, Synergistic effect of dual-doped carbon on Mo_2C nanocrystals facilitates alkaline hydrogen evolution, Nano-Micro Lett. 15 (2023) 166, https://doi.org/10.1007/s40820-023-01135-0.

[6] X. Wang, W. Zhou, Y. Wang, L. Gong, X. Liu, X. Zhou, MoO_2-Mo heterostructures for hydrogen evolution reaction and ammonia sensing in self-powered mode, Nano Energy 109 (2023) 108253, https://doi.org/10.1016/j.nanoen.2023.108253.

[7] Y. Feng, X. Wang, J. Ma, N. Wang, Q. Liu, K. Suenaga, W. Chen, J. Zhang, Y. Zhou, J. Wang, A solid-solution with asymmetric Ni-O-Cr sites for boosting protonation toward anodic oxidation, Adv. Energy Mater. 14 (2024) 2401501, https://doi.org/10.1002/aenm.202401501.

[8] M. Ning, F. Zhang, L. Wu, X. Xing, D. Wang, S. Song, Q. Zhou, L. Yu, J. Bao, S. Chen, Z. Ren, Boosting efficient alkaline fresh water and seawater electrolysis via electrochemical reconstruction, Energy Environ. Sci. 15 (2022) 3945–3957, https://doi.org/10.1039/d2ee01094a.

[9] D. Li, R. Cai, D. Zheng, J. Ren, C. Dong, Y. Huang, S. Haigh, X. Liu, F. Gong, Y. Liu, A sustainable route to ruthenium phosphide (RuP)/Ru heterostructures with electron-shuttling of interfacial Ru for efficient hydrogen evolution, Adv. Sci. 11 (2024) 2309869, https://doi.org/10.1002/advs.202309869.

[10] C. Yang, K. Shen, R. Zhao, H. Xiang, J. Wu, W. Zhong, Q. Zhang, X. Li, N. Yang, Balance effect: a universal strategy for transition metal carbides to enhance hydrogen evolution, Adv. Funct. Mater. 32 (2022) 2108167, https://doi.org/10.1002/adfm.202108167.

[11] H. Lin, Z. Shi, S. He, X. Yu, S. Wang, Q. Gao, Y. Tang, Heteronanowires of MoC-Mo_2C as efficient electrocatalysts for hydrogen evolution reaction, Chem. Sci. 7 (2016) 3399–3405, https://doi.org/10.1039/c6sc00077k.

[12] Y. Chen, B. Gao, M. Wang, X. Xiao, A. Lv, S. Jiao, P.K. Chu, Dual-phase MoC-Mo_2C nanosheets prepared by molten salt electrochemical conversion of CO_2 as excellent electrocatalysts for the hydrogen evolution reaction, Nano Energy 90 (2021) 106533, https://doi.org/10.1016/j.nanoen.2021.106533.

[13] W. Liu, X. Wang, F. Wang, K. Du, Z. Zhang, Y. Guo, H. Yin, D. Wang, A durable and pH-universal self-standing MoC-Mo_2C heterojunction electrode for efficient hydrogen evolution reaction, Nat. Commun. 12 (2021) 6776, https://doi.org/10.1038/s41467-021-27118-6.

[14] Y. Wen, J. Qi, D. Zhao, J. Liu, P. Wei, X. Kang, X. Li, O doping hierarchical NiCoP/Ni_2P hybrid with modulated electron density for efficient alkaline hydrogen

evolution reaction, Appl. Catal. B Environ. 293 (2021) 120196, https://doi.org/10.1016/j.apcatb.2021.120196.
[15] Y. Yang, Y. Qian, H. Li, Z. Zhang, Y. Mu, D. Do, B. Zhou, J. Dong, W. Yan, X. Fan, O-coordinated W-Mo dual-atom catalyst for pH-universal electrocatalytic hydrogen evolution, Sci. Adv. 6 (2020) eaba6586, https://doi.org/10.1126/sciadv.aba6586.
[16] X. Chen, J. Sun, T. Guo, R. Zhao, L. Liu, B. Liu, Y. Wang, J. Li, J. Du, Biomass-derived carbon nanosheets coupled with MoO_2/Mo_2C electrocatalyst for hydrogen evolution reaction, Int. J. Hydrogen Energy 47 (2022) 30959–30969, https://doi.org/10.1016/j.ijhydene.2021.12.173.
[17] Z. Zhang, J. Zhao, M. Wu, Q. Lu, R. Liu, Three-phase interface induced charge modulation on MoO_2/Mo_2C-carbon tube for enhanced hydrogen evolution, Nano Res. 16 (2023) 4706–4714, https://doi.org/10.1007/s12274-022-5140-6.
[18] X. Zhang, T. Chen, N. Lu, F. Jian, B. Zhu, Y. Zhang, L. He, H. Tang, Porous core-shell structured MoO_2-Mo_2C@C electrocatalysts for pH-universal hydrogen evolution reaction, J. Mater. Chem. A 12 (2024) 2036–2043, https://doi.org/10.1039/d3ta06178g.
[19] M. Qiang, X. Zhang, H. Song, C. Pi, X. Wang, B. Gao, Y. Zheng, X. Peng, Paul K. Chu, Kaifu Huo, General synthesis of nanostructured Mo2C electrocatalysts using a carbon template for electrocatalytic applications, Carbon 197 (2022) 238–245, https://doi.org/10.1016/j.carbon.2022.06.016.
[20] C. Wang, X. Li, H. Song, P.K. Chu, K. Huo, In-plane heterostructured MoN/MoC nanosheets with enhanced interfacial charge transfer for superior pseudocapacitive storage, Adv. Funct. Mater. 34 (2024) 2311040, https://doi.org/10.1002/adfm.202311040.
[21] T. Li, J. Yin, D. Sun, M. Zhang, H. Pang, L. Xu, Y. Zhang, J. Yang, Y. Tang, J. Xue, Manipulation of mott-schottky Ni/CeO_2 heterojunctions into N-doped carbon nanofibers for high-efficiency electrochemical water splitting, Small 18 (2022) 2106592, https://doi.org/10.1002/smll.202106592.
[22] F. Ye, D. Chang, A. Ayub, K. Ibrahim, A. Shahin, R. Karimi, S. Wettig, J. Sanderson, K. Musselman, Synthesis of two-dimensional plasmonic molybdenum oxide nanomaterials by femtosecond laser irradiation, Chem. Mater. 33 (2021) 4510–4521, https://doi.org/10.1021/acs.chemmater.1c00732.
[23] B. Deng, Z. Wang, W. Chen, J.T. Li, D.X. Luong, R.A. Carter, G. Gao, B.I. Yakobson, Y. Zhao, J.M. Tour, Phase controlled synthesis of transition metal carbide nanocrystals by ultrafast flash Joule heating, Nat. Commun. 13 (2022) 262, https://doi.org/10.1038/s41467-021-27878-1.
[24] C. Huang, C. Pi, X. Zhang, K. Ding, P. Qin, J. Fu, X. Peng, B. Gao, P.K. Chu, K. Huo, In situ synthesis of MoP nanoflakes intercalated N-doped graphene nanobelts from MoO_3-amine hybrid for high-efficient hydrogen evolution reaction, Small 14 (2018) 1800667, https://doi.org/10.1002/smll.201800667.
[25] Y. Lu, Y. Huang, Y. Zhang, T. Huang, H. Li, J.-j. Cao, W. Ho, Effects of H_2O_2 generation over visible light-responsive Bi/$Bi_2O_{2-x}CO_3$ nanosheets on their photocatalytic NO_x removal performance, Chem. Eng. J. 363 (2019) 374–382, https://doi.org/10.1016/j.cej.2019.01.172.
[26] J. Wang, W. He, Y. Zong, Y. Tang, J. Wang, R. Ma, Electronic redistribution induced by interaction between ruthenium nanoparticles and Ni-N(O)-C sites boosts alkaline water electrolysis, Chem. Commun. 60 (2024) 9444–9447, https://doi.org/10.1039/D4CC02851A.
[27] P. Delporte, F.d.r. Meunier, C. Pham-Huu, P. Vennegues, M.J. Ledoux, J. Guille, Physical characterization of molybdenum oxycarbide catalyst; TEM, XRD and XPS, Catal. Today 23 (1995) 251–267, https://doi.org/10.1016/0920-5861(94)00166-Y.
[28] Z. Zhu, L. Luo, Y. He, M. Mushtaq, J. Li, H. Yang, Z. Khanam, J. Qu, Z. Wang, M. Sadeeq Balogun, High-performance alkaline freshwater and seawater hydrogen catalysis by sword-head structured Mo_2N-Ni_3Mo_3N tunable interstitial compound electrocatalysts, Adv. Funct. Mater. 34 (2023) 2306061, https://doi.org/10.1002/adfm.202306061.
[29] Y. Hu, M. Tu, T. Xiong, Y. He, M. Mushtaq, H. Yang, Z. Khanam, Y. Huang, J. Deng, M. Sadeeq Balogun, Thermal strain engineering in cobalt-coordinated Mo_2N for efficient ampere-level current density alkaline fresh/seawater hydrogen evolution electrocatalysis, J. Energy Chem. 103 (2025) 282–293, https://doi.org/10.1016/j.jechem.2024.11.045.
[30] S. Zhu, C. Wang, H. Shou, P. Zhang, P. Wan, X. Guo, Z. Yu, W. Wang, S. Chen, W. Chu, L. Song, In situ architecting endogenous heterojunction of MoS_2 coupling with Mo_2CT_x MXenes for optimized Li^+ storage, Adv. Mater. 34 (2022) 2108809, https://doi.org/10.1002/adma.202108809.
[31] F. Hu, X. Wang, S. Bao, L. Song, S. Zhang, H. Niu, B. Fan, R. Zhang, H. Li, Tailoring electromagnetic responses of delaminated $Mo_2TiC_2T_x$ MXene through the decoration of Ni particles of different morphologies, Chem. Eng. J. 440 (2022) 135855, https://doi.org/10.1016/j.cej.2022.135855.
[32] Z. Wang, L. Zhang, T.U. Schülli, Y. Bai, S.A. Monny, A. Du, L.J.A.C. Wang, Identifying copper vacancies and their role in the CuO based photocathode for water splitting, Angew. Chem. Int. Ed. 131 (2019) 17768–17773, https://doi.org/10.1002/ange.201909182.
[33] H. Yang, X. Chen, G. Hu, W.-T. Chen, S.J. Bradley, W. Zhang, G. Verma, T. Nann, D.-e. Jiang, P.E. Kruger, X. Wang, H. Tian, G.I.N. Waterhouse, S.G. Telfer, S. Ma, Highly efficient electrocatalytic hydrogen evolution promoted by O-Mo-C interfaces of ultrafine β-Mo_2C nanostructures, Chem. Sci. 11 (2020) 3523–3530, https://doi.org/10.1039/D0SC00427H.
[34] N. Yao, R. Meng, F. Wu, Z. Fan, G. Cheng, W. Luo, Oxygen-vacancy-induced CeO_2/Co_4N heterostructures toward enhanced pH-Universal hydrogen evolution reactions, Appl. Catal. B Environ. 277 (2020) 119282, https://doi.org/10.1016/j.apcatb.2020.119282.
[35] L. Wang, Z. Li, K. Wang, Q. Dai, C. Lei, B. Yang, Q. Zhang, L. Lei, M.K.H. Leung, Y. Hou, Tuning d-band center of tungsten carbide via Mo doping for efficient hydrogen evolution and Zn-H_2O cell over a wide pH range, Nano Energy 74 (2020) 104850, https://doi.org/10.1016/j.nanoen.2020.104850.
[36] L. Dai, F. Yao, L. Yu, C. Fang, J. Li, L. Xue, S. Zhang, P. Xiong, Y. Fu, J. Sun, J. Zhu, Boosting alkaline hydrogen evolution on stoichiometric molybdenum carbonitride via an interstitial vacancy-elimination strategy, Adv. Energy Mater. 12 (2022) 2200974, https://doi.org/10.1002/aenm.202200974.
[37] Z. Wu, Y. Feng, Z. Qin, X. Han, X. Zheng, Y. Deng, W. Hu, Bimetallic multi-level layered Co-NiOOH/Ni_3S_2@NF nanosheet for hydrogen evolution reaction in alkaline medium, Small 18 (2022) 2106904, https://doi.org/10.1002/smll.202106904.
[38] Y. Park, J. Jeong, M. Jang, C. Kwon, G. Kim, J. Jeong, J. Lee, J. Lee, S. Choi, Ternary layered double hydroxide oxygen evolution reaction electrocatalyst for anion exchange membrane alkaline seawater electrolysis, J. Energy Chem. 75 (2022) 127–134, https://doi.org/10.1016/j.jechem.2022.08.011.
[39] Y. Zhang, P. Guo, S. Guo, X. Xin, Y. Wang, W. Huang, M. Wang, B. Yang, A. Jorge Sobrido, J.B. Ghasemi, J. Yu, X. Li, Gradient heating epitaxial growth gives well lattice-matched Mo_2C-Mo_2N heterointerfaces that boost both electrocatalytic hydrogen evolution and water vapor splitting, Angew. Chem. Int. Ed. 61 (2022) e202209703, https://doi.org/10.1002/anie.202209703.
[40] Y. Wang, S. Zheng, We Yang, R. Zhou, Q. He, P. Radjenovic, J. Dong, S. Li, J. Zheng, Z. Yang, In situ raman spectroscopy reveals the structure and dissociation of interfacial water, Nature 600 (2021) 81–85, https://doi.org/10.1038/s41586-021-04068-z.

Supporting Information

MoOC-Mo_2C/C Heterojunction Enables Fast Water Dissociation for Efficient Alkaline Hydrogen Evolution Reaction

Yulei Ren [a], Xuming Zhang [a,*], Hao Song [a,*], Chaoran Pi [a], Jianping Li [a], Xingju Liu [c], Chan Lin [c], Pengcheng Wei [c], Zhuo Li [a,*], Paul K. Chu [b]

[a] The State Key Laboratory of Refractories and Metallurgy and Institute of Advanced Materials and Nanotechnology, Wuhan University of Science and Technology, Wuhan 430081, China

[b] Department of Physics, Department of Materials Science and Engineering, and Department of Biomedical Engineering, City University of Hong Kong, Tat Chee Avenue, Kowloon, Hong Kong, China

[c] Guizhou Wujiang Hydropower Development Co, LTD, Guiyang 550002, China

Electrochemical Measurements

The electrochemical measurements were performed using the conventional three-electrode system in the VSP-300 type electrochemical workstation (Biologic Science Instruments, France). The MoOC-Mo_2C/C NBs on carbon cloth (CC) (1×1 cm^2 in size) with a mass loading of 5.2 mg cm^{-2} served as the working electrode and a carbon rod was the counter electrode. The reference electrode was Hg/HgO (1.0 M KOH). In the electrochemical test, all the potentials were corrected with automatic 85% iR-compensation and converted to the standard reversible hydrogen electrode (RHE).

Linear sweep voltammetry (LSV) was carried out at a scanning rate of 5 mV s^{-1}. Cyclic voltammetry (CV) was performed at a scanning rate of 100 mV s^{-1} for 5,000 cycles in the selected potential ranges. Before and after cycling, the polarization curves were recorded under quasi-equilibrium conditions at a scanning rate of 5 mV s^{-1}. The electrochemical double-layer capacitance (C_{dl}) was measured based on the CVs acquired at different scanning rates from 5 to 50 mV s^{-1} in the non-Faradic region. Electrochemical impedance spectroscopy (EIS) was conducted at an overpotential of 40 mV in the frequency range between 100 kHz and 10 mHz with an AC perturbation of 5 mV. The overall water electrolysis was assessed on a standard two-electrode system with MoOC-Mo_2C/C NBs as the cathode and NiFe LDH/NF as the anode in 1.0 M KOH.

The Faradaic Efficiency (η_F**)** can be calculated by the following equation:

$$\eta_F = \frac{m \times n \times F}{I \times t} \times 100\%$$

where m, n, F, I and t are the molar amount of the relevant product, number of electrons transferred in the reaction, Faraday's constant (96485 C mol-1), average current density and reaction time, respectively.

The double-layer capacitance (C_{dl}) can be calculated by the following equation:

$$\Delta j = vC_{dl}$$

where v is the scan rate and Δj is half of the current density difference in the CV curve ($\Delta j = (j_a - j_c)/2$).

The electrochemically active surface area (ECSA) is linearly related to C_{dl}, and ECSA can be deduced from C_{dl} using the following equation:

$$ECSA = C_{dl} / C_s$$

where C_s represents the specific capacitance per unit area of surface under certain conditions.

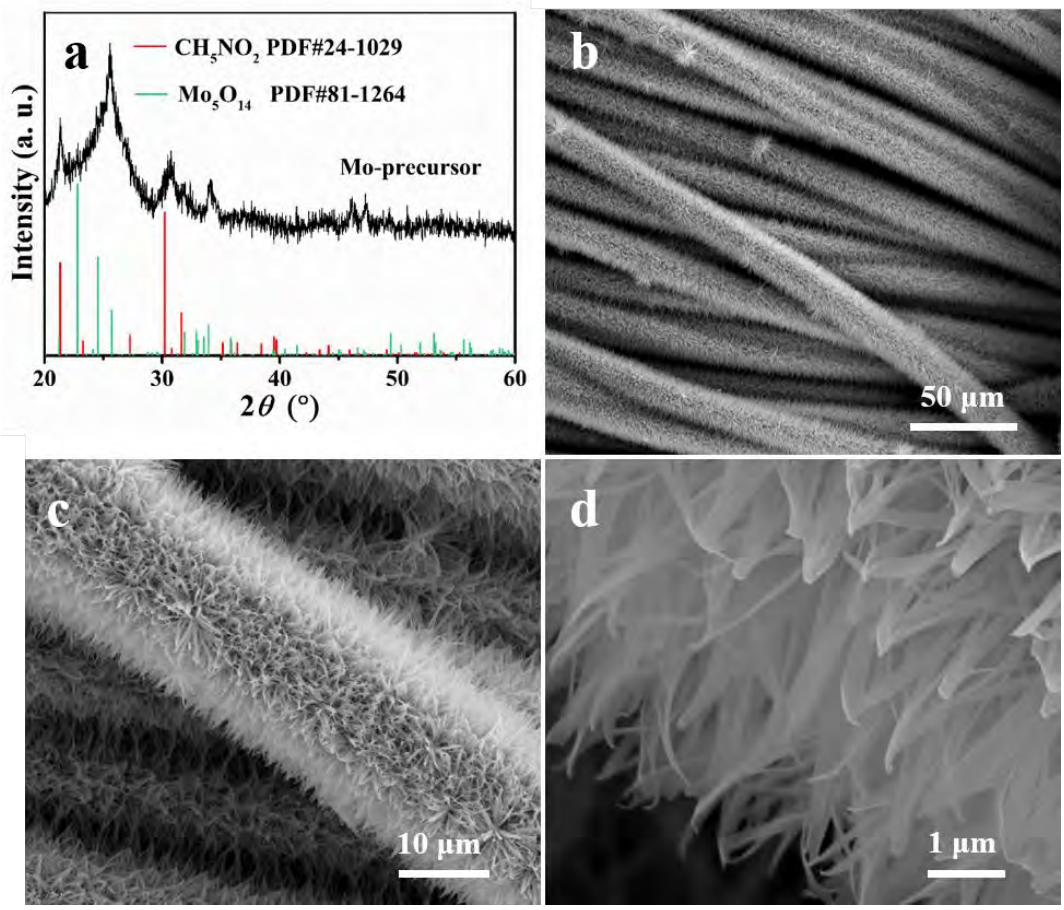

Figure S1. (a) XRD pattern and (b-d) Low and high magnified SEM images of Mo-based precursor.

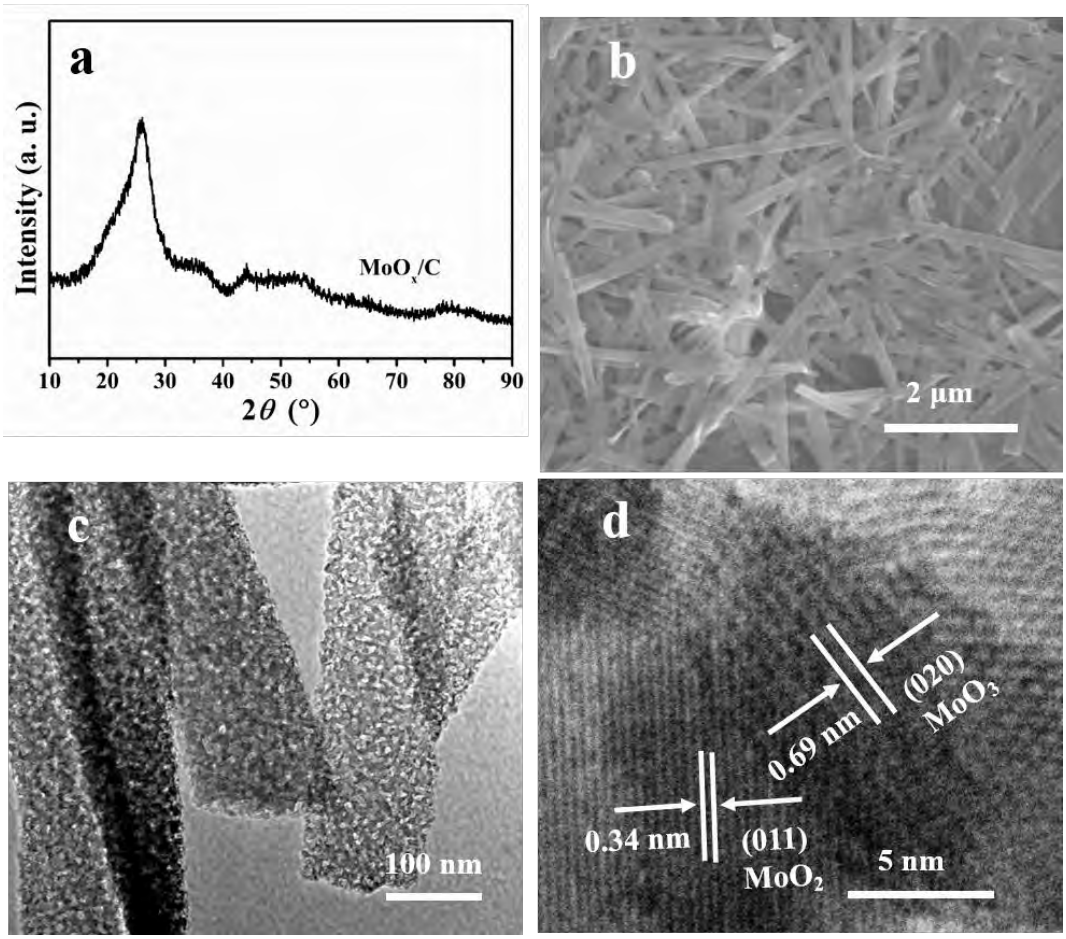

Figure S2. (a-b) XRD pattern and SEM image, (c-d) Low and high magnified TEM images of MoO_x/C NBAs.

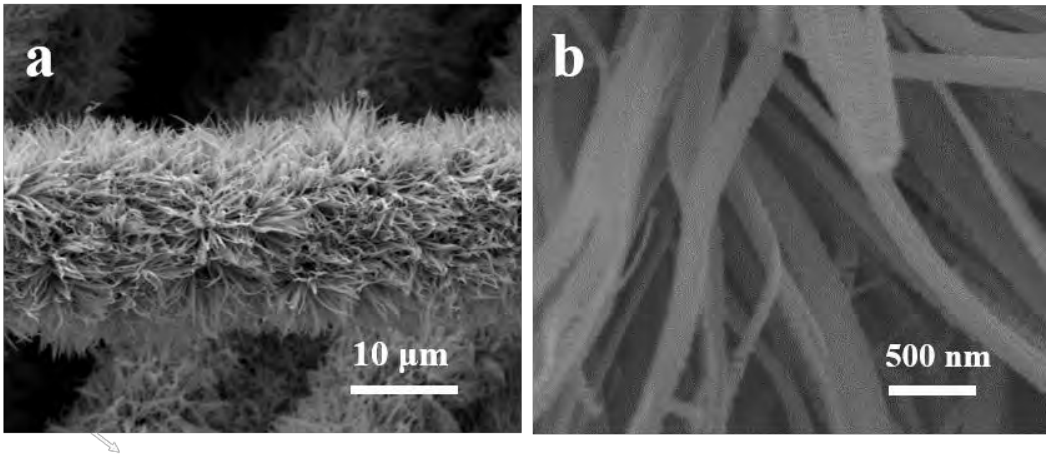

Figure S3. (a) The SEM image of Mo_2C/C NBs.

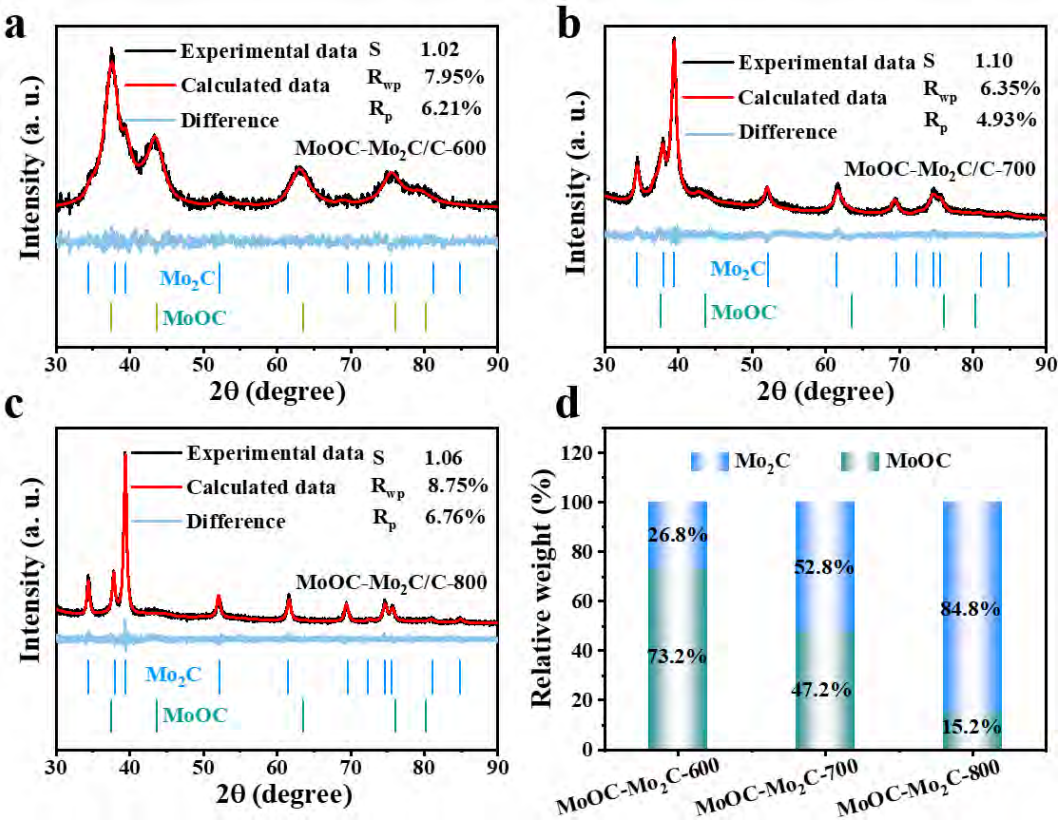

Figure S4. (a-c) XRD Rietveld refinement analysis of MoOC-Mo_2C/C-600, MoOC-Mo_2C/C-700, and MoOC-Mo_2C/C-800. (d) Corresponding relative weight of MoOC and Mo_2C by Rietveld refinement analysis.

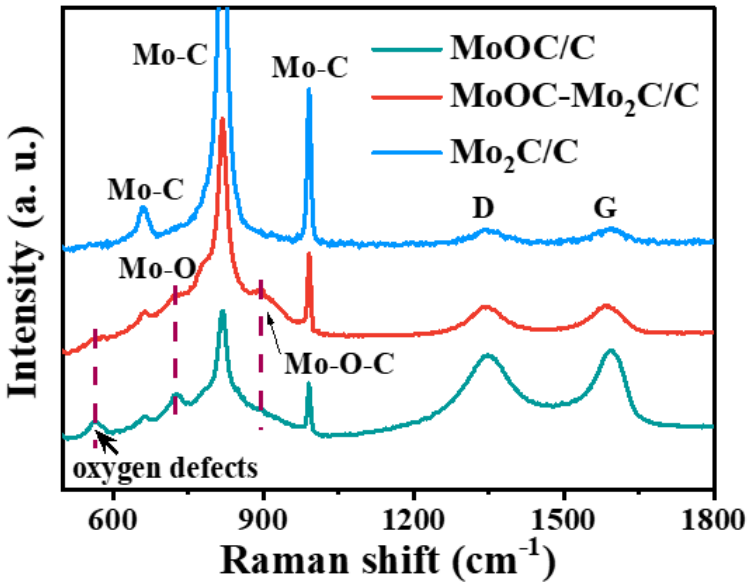

Figure S5. Raman spectrum of MoOC/C, MoOC-Mo_2C/C, and Mo_2C/C.

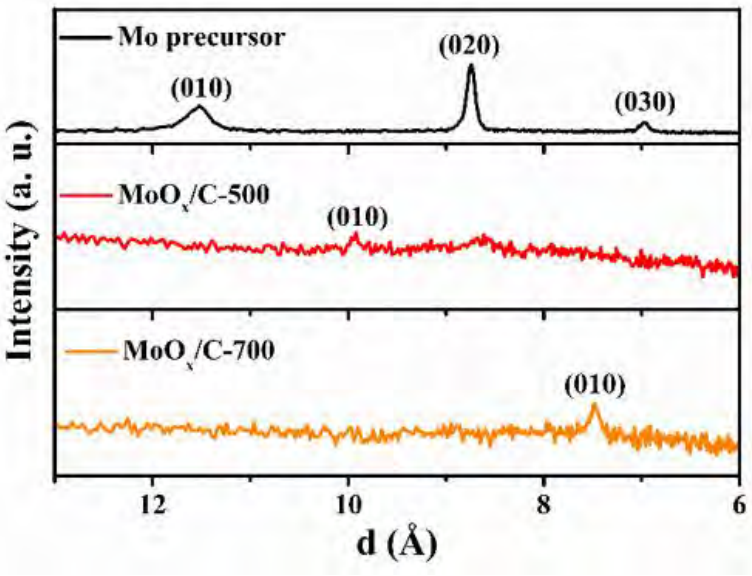

Figure S6. Small-angle XRD patterns with the interlayer spacing of Mo-based precursor, MoO_x/C-500, and MoO_x/C-700 NBs.

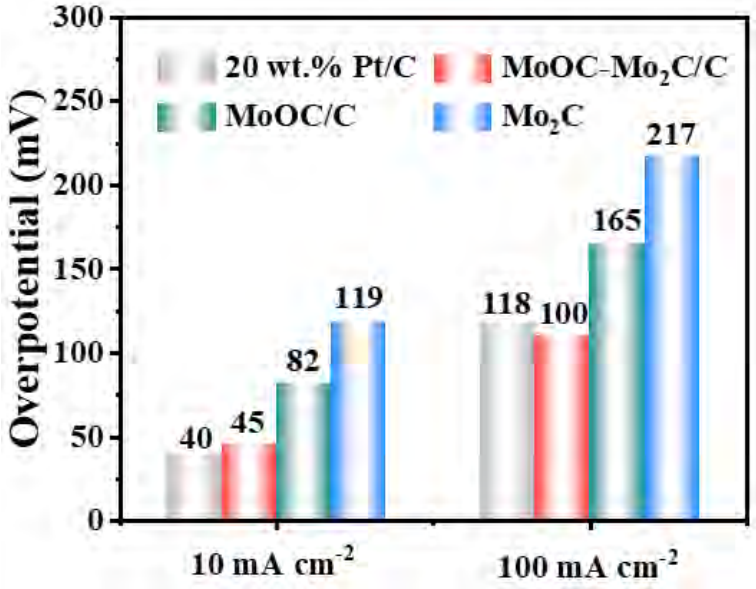

Figure S7. Overpotentials of Mo_2C/C, MoOC/C, and MoOC-Mo_2C/C electrodes.

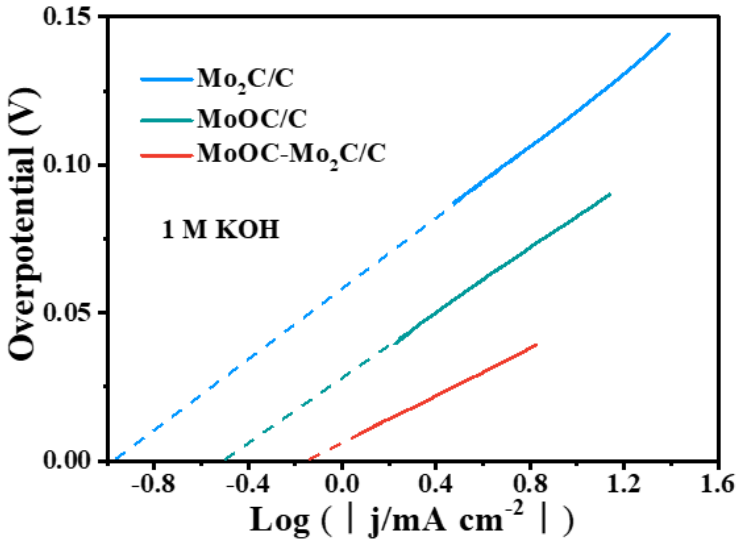

Figure S8. Exchange current densities (j0) of Mo_2C/C, MoOC/C, and MoOC-Mo_2C/C.

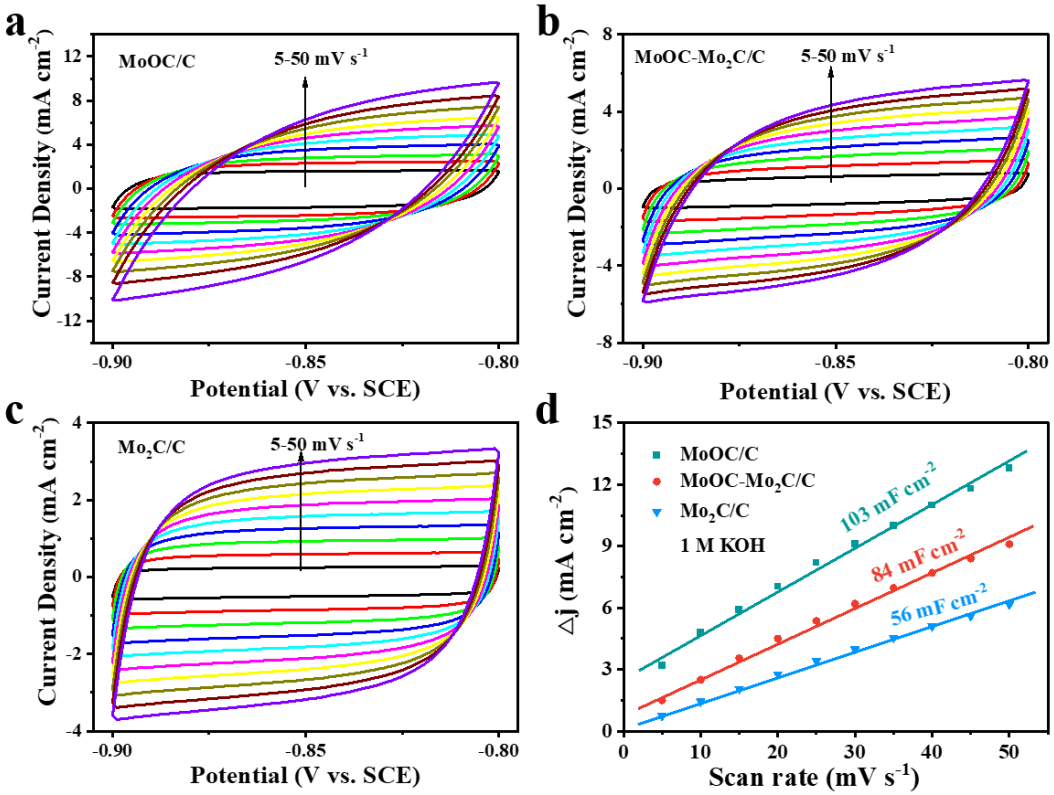

Figure S9. Electrochemical capacitance measurements: (a) MoOC/C, (b) MoOC-Mo_2C/C and (c) Mo_2C/C and in 1 M KOH media. (d) Plots showing extraction of the double-layer capacitance (C_{dl}).

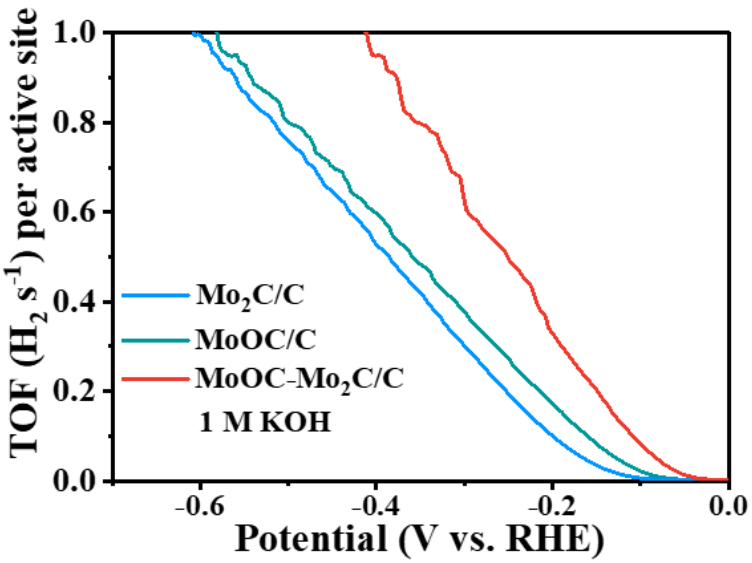

Figure S10. TOF curves of MoOC/C, Mo_2C/C, and MoOC-Mo_2C/C in 1 M KOH.

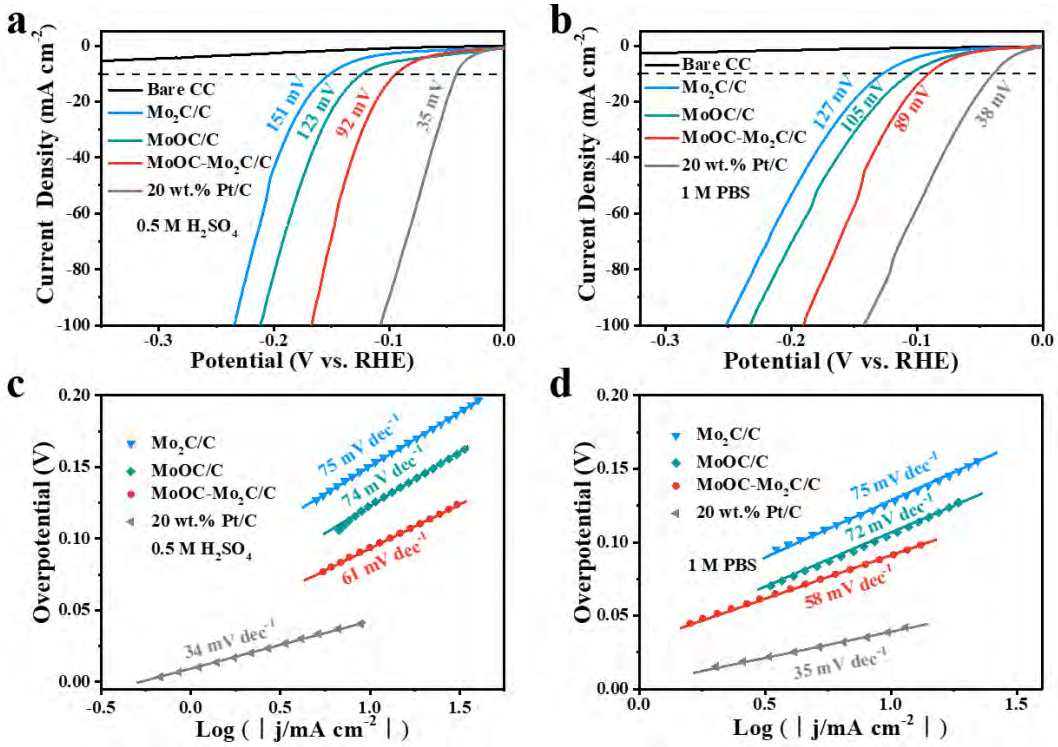

Figure S11. Polarization curves of the bare CC, Mo_2C/C, MoOC/C, MoOC-Mo_2C/C, and commercial 20 wt.% Pt/C in (a) 0.5 M H_2SO_4 and (b) 1 M PBS. (b) Corresponding Tafel plots.

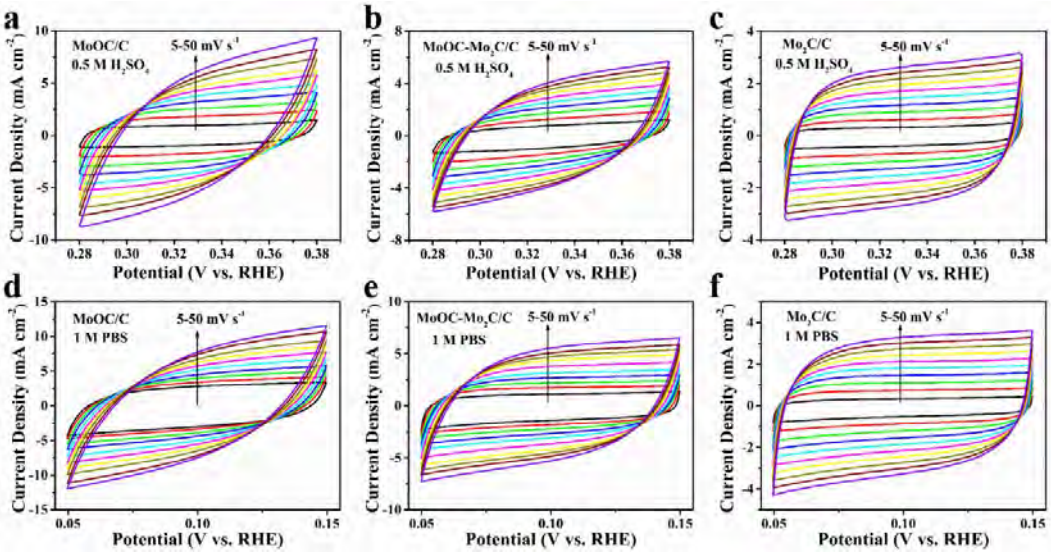

Figure S12. Electrochemical capacitance measurements: (a) MoOC/C, (b) MoOC-Mo_2C/C, and (c) Mo_2C/C in 0.5 M H_2SO_4. And (d) MoOC/C, (e) MoOC-Mo_2C/C, and (f) Mo_2C/C in 1 M PBS.

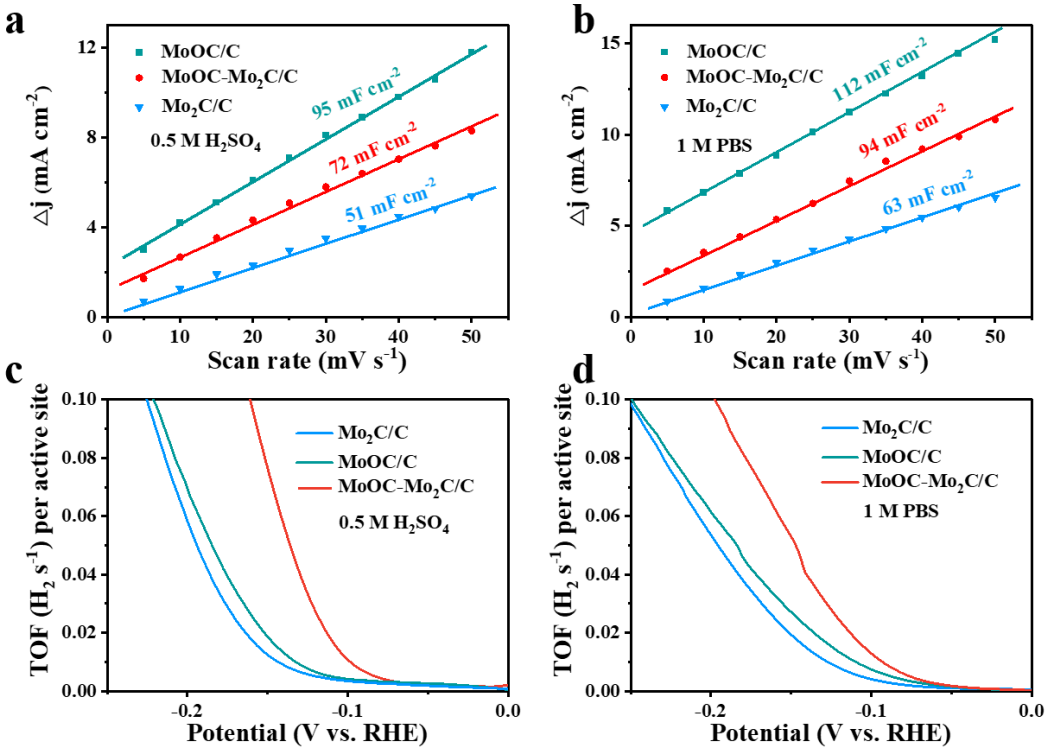

Figure S13. The double-layer capacitance (Cdl) and TOF curves of Mo_2C/C, MoOC/C and MoOC-Mo_2C/C in (a,c) 0.5 M H_2SO_4 and (b, d) 1 M PBS.

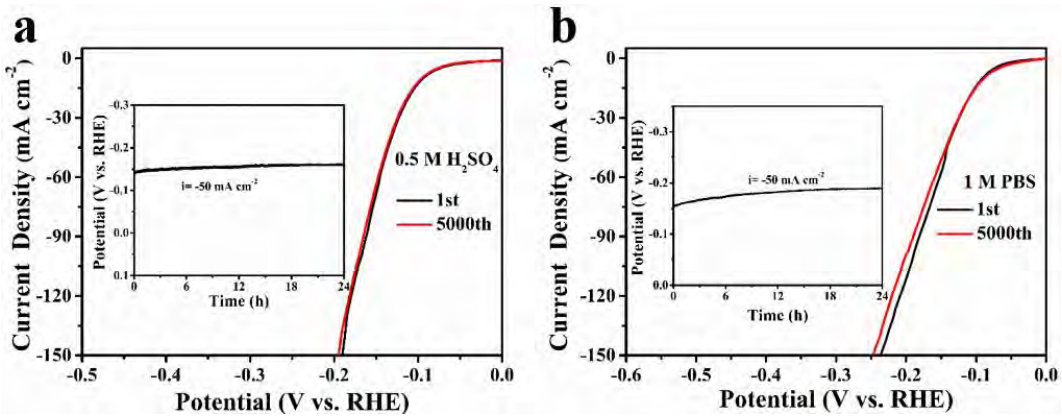

Figure S14. Polarization curves at the first and last 5,000th cycles of MoOC-Mo_2C/C with the insets showing the long-term test of the i-t curve of MoOC-Mo_2C/C in (a) 0.5 M H_2SO_4 and (b) 1 M PBS.

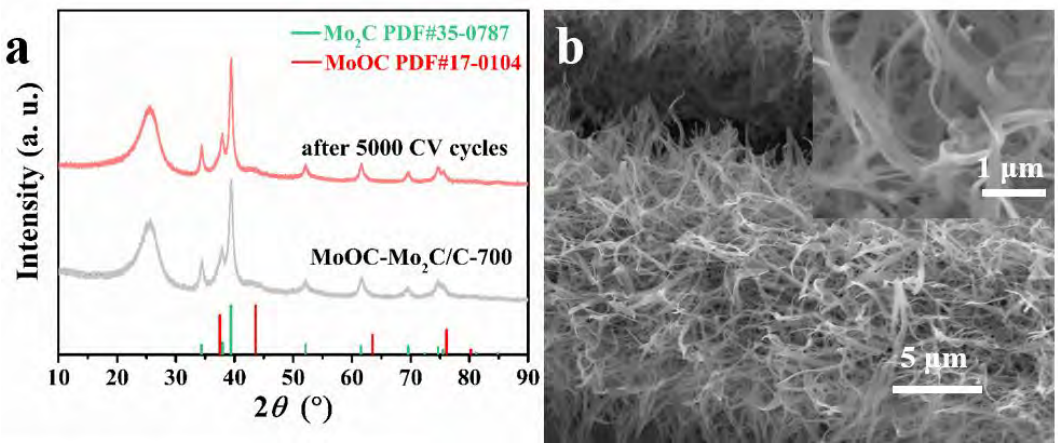

Figure S15. (a) XRD patterns of MoOC-Mo_2C/C after 5000 CV cycles and (b) SEM images after I-t tests at -100 mA cm^{-2} for over 24 h.

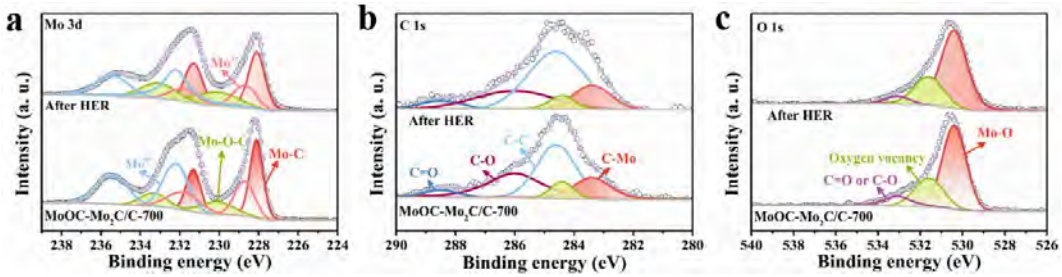

Figure S16. (a) High-resolution Mo 3d, (b) C 1s, and (c) O 1s XPS spectra of MoOC-Mo_2C/C before and after HER at 110 mV for 24 h.

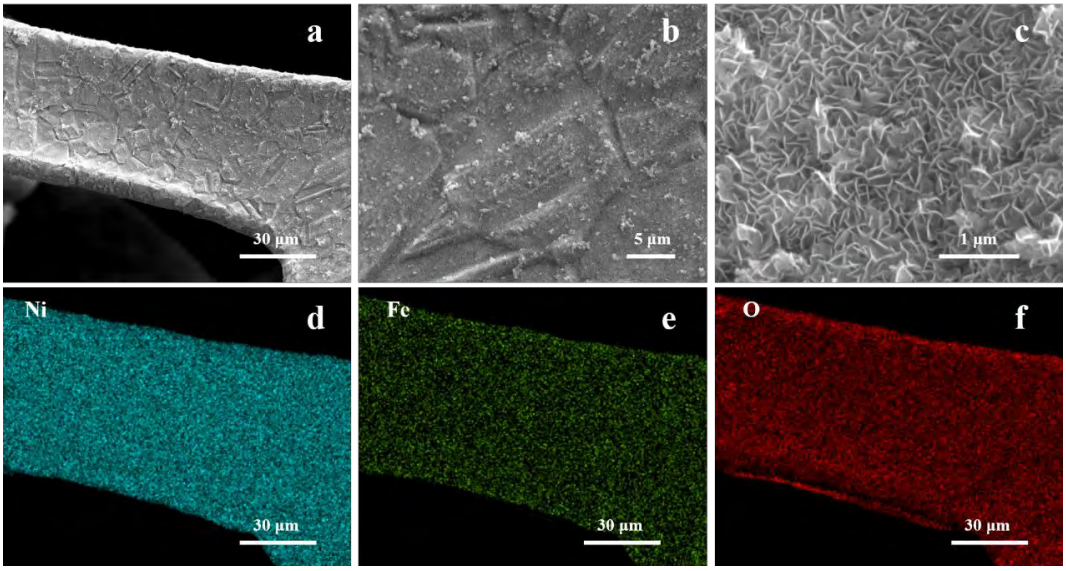

Figure S17. (a-c) The SEM images and (d-e) EDS elemental maps of NiFe-LDH.

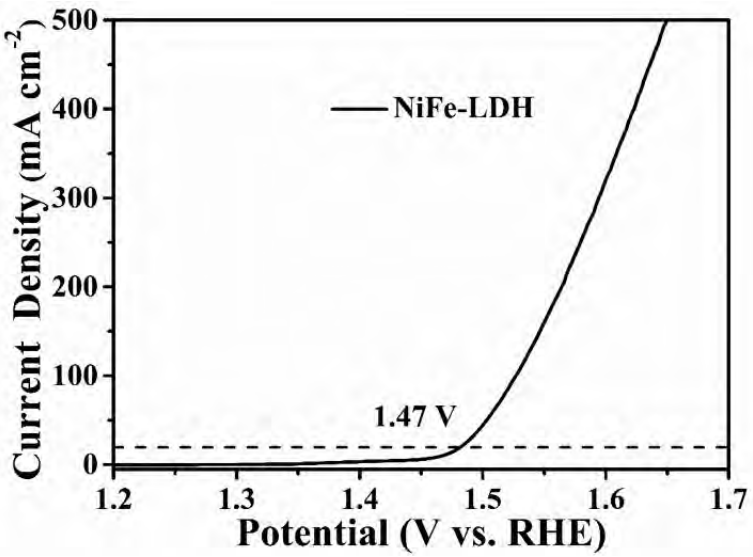

Figure S18. The OER LSV curves of NiFe-LDH.

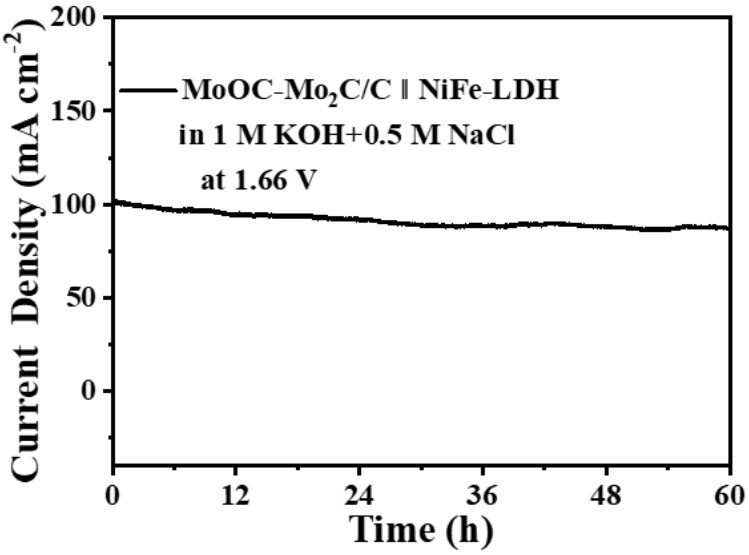

Figure S19. Chronopotentiometry tests of MoOC-Mo_2C/C for OWS at 100 mA cm^{-2}.

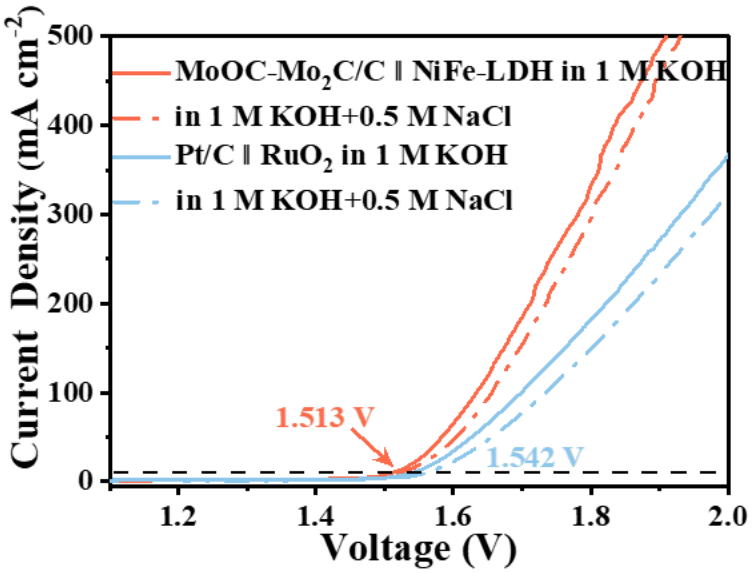

Figure S20. Polarization curves of MoOC-Mo_2C/C||NiFe-LDH and Pt/C||RuO_2 for overall water splitting in 1 M KOH and 1 M KOH + 0.5 M NaCl electrolytes.

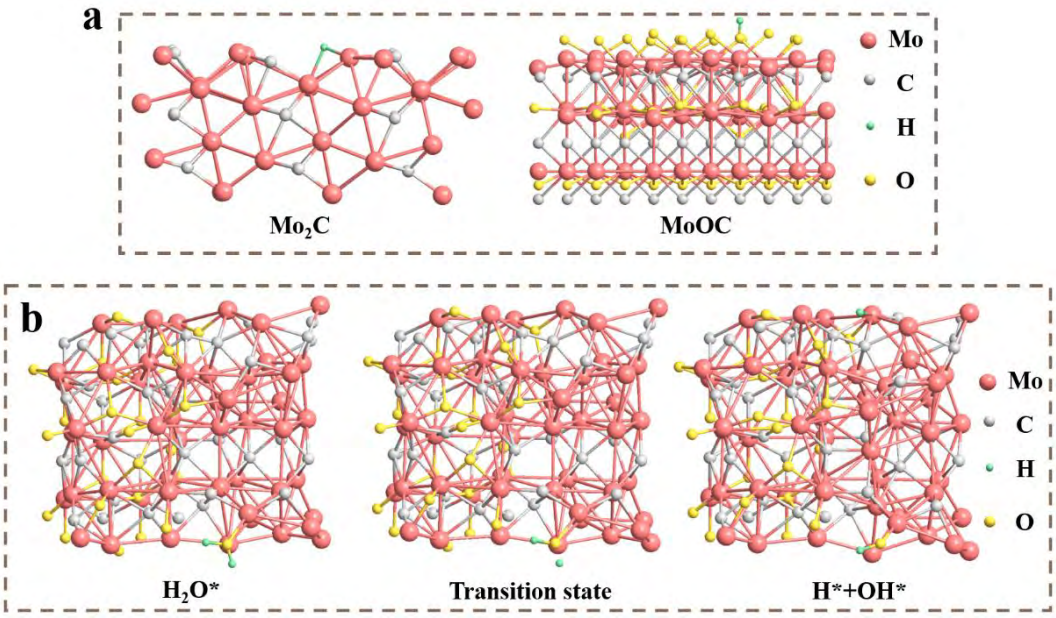

Figure S21. The schematic models of Mo_2C and MoOC (a) with H adatom and (b) for the water dissociation process.

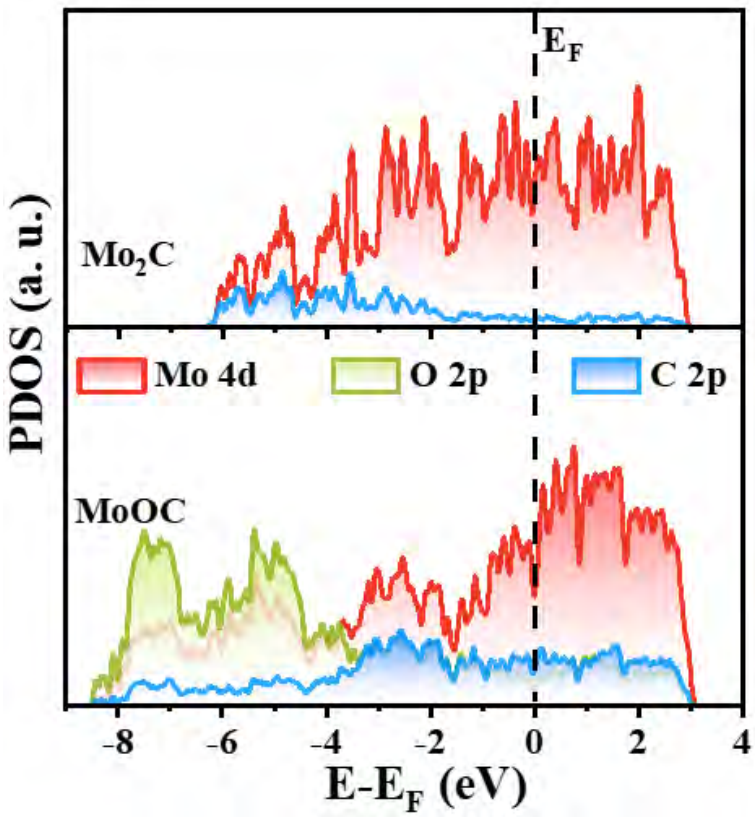

Figure S22. PDOS plots of Mo_2C and MoOC.

Table S1 The impedance fitting results for different samples

Samples	MoOC/C	Mo_2C/C	MoOC-Mo_2C/C
Rs (Ω)	1.6	1.8	1.7
C_{dl} (mF)	451.2	38.6	239.7
R_{ct} (Ω)	11.9	22.1	3.1

Table S2. Comparison of the HER performance of MoOC-Mo_2C/C with other electrocatalysts recently reported in 1 M KOH media.

Catalysts	load mass (mg cm^{-2})	η_{10} (mV)	Tafel slopes (mV dec^{-1})	η_{500} (mV)	Reference
MoOC-Mo_2C/C	**5.2**	**45**	**38**	**255**	**This work**
MoC-Mo_2C	−−	98.2	59	292	Nat. Commun. 12 (2021) 6776
Fe-Mo-S/Ni_3S_2@NF	2.22	141	123	384	Chem. Eng. J. 404 (2021) 126483
$MoSe_2$-Mo_2N/Mo	−−	76	69.5	~320	J Mater. Chem. A, 9 (2021) 26113-26118
HC-MoS_2/Mo_2C	10	N/A	60	~390	Nat. Commun. 11 (2020) 3724
MoS_2-Mo_2C	−−	56	64.2	~310	Chem. Commun., 57 (2021) 11819-11822
Ni_2P-Fe_2P/NF	16	41	86	298	Adv. Funct. Mater. 31 (2021) 2006484
$CoMoS_x$/NF	−−	89	94	269	Angew. Chem. Int. Ed. 59 (2020) 1659-1665
NC/Ni_3Mo_3N/NF	0.357	168	41.5	~400	Appl. Catal. B Environ. 272 (2020) 118956
MnO_x/NiFeP/NF	−−	N/A	41.8	255	Small 18 (2022) 2105803
$Ni_{56.5}Co_{35}Ti_{8.5}$	−−	230	82	425	ACS Catal. 12 (2022) 3789-3796

Table S3. Comparison of the HER performance of MoOC-Mo_2C/C with other electrocatalysts recently reported in 0.5 M H_2SO_4 and 1 M PBS electrolytes.

Catalysts	load mass (mg cm^{-2})	Electrolyte	η_{10} (mV)	Tafel slopes (mV dec^{-1})	Reference
MoOC-Mo_2C/C	**5.2**	**0.5 M H_2SO_4**	**92**	**61**	**This work**
		1 M PBS	**89**	**58**	
Mo-MoS_2 HMS/CP	0.21	0.5 M H_2SO_4	91	61.9	Nano Energy 101 (2022) 107563
		1 M PBS	128	74.5	
S-Mo_2C	3.0	0.5 M H_2SO_4	98	54.6	Appl. Catal. B Environ. 322 (2023) 122131
		1 M PBS	161	86.3	
MoC/Mo_2C	– –	0.5 M H_2SO_4	153	72.9	ACS Sustainable Chem. Eng. 11 (2023) 3585-3593
		1 M PBS	181	-	
Mo@(2H-1T)-$MoSe_2$	2.82	0.5 M H_2SO_4	~163	72	Appl. Catal. B Environ. 304 (2022) 120993
		1 M PBS	~210	89	
MoO_2-Mo_2C-NC	– –	0.5 M H_2SO_4	72	56.42	Chem. Eng. J. 469 (2023) 143908
		1 M PBS	206	59.7	
Mo/MoO_2	3	0.5 M H_2SO_4	108	68	J. Colloid Interf. Sci. 608 (2022) 1696-1706
		1 M PBS	164	107	

Table S4. Comparison of catalytic performance for alkaline water electrolysis.

Cathode	load mass (mg cm^{-2})	Anode	Electrolyte	Cell voltage (V) at 100 mA cm^{-2}	Reference
$MoOC-Mo_2C/C$	**5.2**	**NiFe-LDH**	**1 M KOH**	**1.633**	**This work**
			1 M KOH +0.5 M NaCl	**1.656**	
Ni_2P-FeP/FF	– –	Ni-Fe LDH/FF	1 M KOH +0.5 M NaCl	~1.68	Nano Res. (2022) 1-7
S,P-(Ni,Mo,Fe)OOH/NiMoP	1	S,P-(Ni,Mo,Fe)OOH/NiMoP	1 M KOH	1.691	Appl. Catal. B: Environ. 293 (2021) 120215
			1 M KOH +0.5 M NaCl	1.703	
Mo-CoP_x/NF	5	Mo-CoP_x/NF	1 M KOH	2.01	Materials Today Nano 18 (2022) 100216
			1 M KOH +0.5 M NaCl	1.95	
S-$NiMoO_4$@NiFe-LDH	– –	S-$NiMoO_4$@NiFe-LDH	1 M KOH +0.5 M NaCl	1.68	J. Colloid Interf. Sci. 613 (2022) 349-358
Ni/Mo_2C-NCS	– –	Fe/Mo_2C-NCS	1 M KOH	1.66	Chem. Eng. J. 431 (2022) 134126
Pt/C	– –	$Co_{1.98}$-NiFe LDH	1 M KOH	1.82	Appl. Catal. B: Environ. 314 (2022) 121491
			1 M KOH +1 M NaCl	1.84	
FeP@CoP/NF	13.3	NiFe LDH@Co_3O_4/NF	1 M KOH +0.5 M NaCl	1.74	Appl. Catal. B: Environ. 317 (2022) 121799
NiP_2-FeP_2/Cu_{NW}/CF	1.5	NiFe-LDH	1 M KOH	~1.76	ACS Energy Lett. 6 (2021) 354
P-MoP/Mo_2N	– –	NiFe-LDH	1 M KOH	~1.82	Nat. Commun. 12 (2021) 6776
Co/Mo_2C@C	0.336	Co/Mo_2C@C	1 M KOH	1.84	Chem. Eng. J. 430 (2022) 132697

Reference

[1] W. Liu, X. Wang, F. Wang, K. Du, Z. Zhang, Y. Guo, H. Yin, D. Wang, A durable and pH-universal self-standing MoC-Mo_2C heterojunction electrode for efficient hydrogen evolution reaction, Nat. Commun. 12 (2021) 6776, https://doi.org/10.1038/s41467-021-27118-6.

[2] Y. Zhang, H. Guo, X. Li, J. Du, W. Ren, R. Song, A 3D multi-interface structure of coral-like Fe-Mo-S/Ni_3S_2@NF using for high-efficiency and stable overall water splitting, Chem. Eng. J. 404 (2021) 126483, https://doi.org/10.1016/j.cej.2020.126483.

[3] C. Jian, W. Hong, Q. Cai, W. Liu, The local electronic structure modulation of the molybdenum selenide-nitride heterojunction for efficient hydrogen evolution reaction, J Mater. Chem. A 9 (2021) 26113-26118, https://doi.org/10.1039/d1ta07533k.

[4] C. Zhang, Y. Luo, J. Tan, Q. Yu, F. Yang, Z. Zhang, L. Yang, H. Cheng, B. Liu, High-throughput production of cheap mineral-based two-dimensional electrocatalysts for high-current-density hydrogen evolution, Nat. Commun. 11 (2020) 3724, https://doi.org/10.1038/s41467-020-17121-8.

[5] C. Jian, Q. Cai, W. Liu, A three-dimensional macroporous framework molybdenum disulfide-carbide heterojunction for highly efficient electrocatalytic hydrogen evolution at high current densities, Chem. Commun. 57 (2021) 11819-11822, https://doi.org/10.1039/d1cc04431a.

[6] L. Wu, L. Yu, F. Zhang, B. McElhenny, D. Luo, A. Karim, S. Chen, Z. Ren, Heterogeneous bimetallic phosphide Ni_2P-Fe_2P as an efficient bifunctional catalyst for water/seawater splitting, Adv. Funct. Mater. 31 (2021) 2006484, https://doi.org/10.1002/adfm.202006484.

[7] X. Shan, J. Liu, H. Mu, Y. Xiao, B. Mei, W. Liu, G. Lin, Z. Jiang, L. Wen, L. Jiang, An engineered superhydrophilic/superaerophobic electrocatalyst composed of the supported $CoMoS_x$ chalcogel for overall water splitting, Angew. Chem. Int. Ed. 59 (2020) 1659-1665, https://doi.org/10.1002/anie.201911617.

[8] Y. Chen, J. Yu, J. Jia, F. Liu, Y. Zhang, G. Xiong, R. Zhang, R. Yang, D. Sun, H. Liu, W. Zhou, Metallic Ni_3Mo_3N porous microrods with abundant catalytic sites as efficient electrocatalyst for large current density and superstability of hydrogen evolution reaction and water splitting, Appl. Catal. B Environ. 272 (2020) 118956, https://doi.org/10.1016/j.apcatb.2020.118956.

[9] P. Wang, Y. Luo, G. Zhang, M. Wu, Z. Chen, S. Sun, Z. Shi, MnO_x-decorated nickel-iron phosphides nanosheets: interface modifications for robust overall water splitting at ultra-high current densities, Small, 18 (2022) 2105803, https://doi.org/10.1002/smll.202105803.

[10] X. Liu, P. Zou, L. Song, B. Zang, B. Yao, W. Xu, F. Li, J. Schroers, J. Huo, J. Wang, Combinatorial high-throughput methods for designing hydrogen evolution reaction catalysts, ACS Catal. 12 (2022) 3789-3796, https://doi.org/10.1021/acscatal.2c00869.

[11] Z. Sun, L. Lin, M. Yuan, H. Yao, Y. Deng, B. Huang, H. Li, G. Sun, J. Zhu, Mott-

Schottky heterostructure induce the interfacial electron redistribution of MoS_2 for boosting pH-universal hydrogen evolution with Pt-like activity, Nano Energy, 101 (2022) 107563, https://doi.org/10.1016/j.nanoen.2022.107563.

[12] M. Hu, B. Liu, H. Chen, X. Xu, P. Jing, X. Guo, R. Yang, X. Wang, R. Gao, J. Zhang, Universal construction of sulfur doped molybdenum-based nanosheets for enhanced hydrogen evolution in a wide pH range, Appl. Catal. B Environ. 322 (2023) 122131, https://doi.org/10.1016/j.apcatb.2022.122131.

[13] Y. Zhang, X. Liu, W. Li, W. Liu, H. Yin, D. Wang, Advanced and durable self-standing MoC-Mo_2C electrode for alkaline hydrogen evolution in chlor-alkali electrolysis, ACS Sustainable Chem. Eng. 11 (2023) 3585-3593, https://doi.org/10.1021/acssuschemeng.3c01721.

[14] C. Yang, L. Zhou, C. Wang, W. Duan, L. Zhang, F. Zhang, J. Zhang, Y. Zhen, L. Gao, F. Fu, Y. Liang, Large-scale synthetic Mo@(2H-1T)-$MoSe_2$ monolithic electrode for efficient hydrogen evolution in all pH scale ranges and seawater, Appl. Catal. B Environ. 304 (2022) 120993, https://doi.org/10.1016/j.apcatb.2021.120993.

[15] J. Huang, Y. Liu, L. Wang, Z. Hou, Z. Zhang, X. Zhang, J. Liu, Coupling interactions enhancing molybdenum-based electrocatalysts for high-efficiency hydrogen evolution at wide pH, Chem. Eng. J. 469 (2023) 143908, https://doi.org/10.1016/j.cej.2023.143908.

[16] G. Yang, Y. Guo, X. Bo, Laser-assisted coupling of nitrogen-doped carbon-coated molybdenum/molybdenum dioxide rods for efficient pH-universal hydrogen evolution electrocatalysis, J. Colloid Interf. Sci. 608 (2022) 1696-1706,

https://doi.org/10.1016/j.jcis.2021.10.088.

[17] J. Li, M. Song, Y. Hu, C. Zhang, W. Liu, X. Huang, J. Zhang, Y. Zhu, J, Zhang, D. Wang, A self-supported heterogeneous bimetallic phosphide array electrode enables efficient hydrogen evolution from saline water splitting, Nano Res. 16 (2023) 3658-3664, https://doi.org/10.1007/s12274-022-4608-8.

[18] H. Chen, Y. Zou, J. Li, K. Zhang, Y. Xia, B. Hui, D. Yang, Wood aerogel-derived sandwich-like layered nanoelectrodes for alkaline overall seawater electrosplitting, Appl. Catal. B: Environ. 293 (2021) 120215, https://doi.org/10.1016/j.apcatb.2021.120215.

[19] Y. Yu, J. Li, J. Luo, Z. Kang, C. Jia, Z. Liu, W. Huang, Q. Chen, P. Deng, Y. Shen, X. Tian, Mo-decorated cobalt phosphide nanoarrays as bifunctional electrocatalysts for efficient overall water/seawater splitting, Mater. Today Nano, 18 (2022) 100216, https://doi.org/10.1016/j.mtnano.2022.100216.

[20] H. Wang, L. Chen, L. Tan, X. Liu, Y. Wen, W. Hou, T. Zhan, Electrodeposition of NiFe-layered double hydroxide layer on sulfur-modified nickel molybdate nanorods for highly efficient seawater splitting, J. Colloid Interf. Sci. 613 (2022) 349-358, https://doi.org/10.1016/j.jcis.2022.01.044.

[21] Y. Xu, J. Yang, T. Liao, R. Ge, Y. Liu, J. Zhang, Y. Li, M. Zhu, S. Li, W. Li, Bifunctional water splitting enhancement by manipulating Mo-H bonding energy of transition metal-Mo_2C heterostructure catalysts, Chem. Eng. J. 431 (2022) 134126, https://doi.org/10.1016/j.cej.2021.134126.

[22] Y. Yang, S. Wei, Y. Li, D. Guo, H. Liu, L. Liu, Effect of cobalt doping-regulated

crystallinity in nickel-iron layered double hydroxide catalyzing oxygen evolution, Appl. Catal. B: Environ. 314 (2022) 121491, https://doi.org/10.1016/j.apcatb.2022.121491.

[23] C. Lyu, J. Cheng, K. Wu, J. Wu, N. Wang, Z. Guo, P. Hu, W. Lau, J. Zheng, Interfacial electronic structure modulation of CoP nanowires with FeP nanosheets for enhanced hydrogen evolution under alkaline water/seawater electrolytes, Appl. Catal. B: Environ. 317 (2022) 121799, https://doi.org/10.1016/j.apcatb.2022.121799.

[24] A. Kumar, V. Bui, J. Lee, A. Jadhav, Y. Hwang, M. Kim, Y. Kawazoe, H. Lee, Modulating interfacial charge density of NiP_2-FeP_2 via coupling with metallic cu for accelerating alkaline hydrogen evolution, ACS Energy Lett. 6 (2021) 354-363, https://doi.org/10.1021/acsenergylett.0c02498.

[25] Y. Gu, A. Wu, Y. Jiao, H. Zheng, X. Wang, Y. Xie, L. Wang, C. Tian, H. Fu, Two-dimensional porous molybdenum phosphide/nitride heterojunction nanosheets for pH-universal hydrogen evolution reaction, Angew. Chem. Int. Ed. 60 (2021) 6673-6681, https://doi.org/10.1002/ange.202016102.

[26] S. Yuan, M. Xia, Z. Liu, K. Wang, L. Xiang, G. Huang, J. Zhang, N. Li, Dual synergistic effects between Co and Mo_2C in Co/Mo_2C heterostructure for electrocatalytic overall water splitting, Chem. Eng. J. 430 (2022) 132697, https://doi.org/10.1016/j.cej.2021.132697.